Spin-wave mediated magnetoelectric effect in YIG/graphene bilayers

Master thesis

Michael Evelt, WWU Münster
Student no. 364267

Supervisor
Prof. Dr. Sergej Demokritov

Münster, Mai 2014

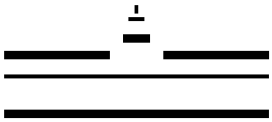

Westfälische
Wilhelms-Universität
Münster

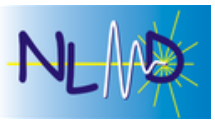

1. Gutachter: Prof. Dr. S. O. Demokritov
2. Gutachter: Dr. V. E. Demidov

Abstract

The topic of this thesis is the experimental examination of the behaviour of yttrium iron garnet (YIG)/graphene bilayers under the influence of spin-wave excitation in the YIG layer. Measurements reveal a voltage in the graphene layer along the direction of propagation that is clearly correlated to the excitation of spin-waves. While this voltage for in-plane magnetized structures can be explained by the Seebeck effect mediated by the damping of spin-waves the situation for out-of-plane magnetized structures is more complex:
Under the reversal of the static magnetic field an additional contribution to the voltage is revealed. This component reverses sign under the inversion of the magnetic field, and its amplitude increases linearly with the absorbed microwave energy. The amplitude of this voltage additionally depends resonantly on the excitation frequency of spin-waves. As the origin of this phenomenon we propose a spin-wave mediated magnetoelectric effect and derive a phenomenological equation.

Zusammenfassung

Thema dieser Masterarbeit ist die experimentelle Untersuchung von Yttrium-Eisen-Granat (YIG)/Graphen Doppelschichten unter Einfluss von Spinwellenanregung in der YIG-Schicht. Messungen zeigen eine Spannung in der Graphenschicht entlang der Propagationsrichtung die eindeutig mit der Anregung von Spinwellen korreliert ist. Während diese Spannung für in der Ebene magnetisierte Doppelschichten durch den Seebeck Effekt, vermittelt durch die Dämpfung von Spinwellen, erklärt werden kann, ist die Situation für aus der Ebene magnetisierte Doppelschichten komplexer: Unter Umkehr des statischen magnetischen Feldes kann ein weiterer Beitrag zur Spannung beobachtet werden. Diese Komponente kehrt ihr Vorzeichen unter Inversion des magnetischen Feldes um und ihre Amplitude steigt linear mit der absorbierten Mikrowellenenergie an. Zusätzlich hängt diese Spannung resonant von der Anregungsfrequenz der Spinwellen ab. Als Ursprung dieses Phänomens schlagen wir einen durch Spinwellen vermittelten magnetoelektrischen Effekt vor und bestimmen eine phänomenologische Formel.

Contents

1 Introduction

The basic question for this master thesis can be defined as follows:
What happens if we combine the best material known for spin-wave propagation and the most promising candidate for future electronics in a bilayer? From the examination of laminated structures one can learn that bilayers contain properties of both layers, but can additionally show combined properties that cannot be observed if each material is regarded independently (see for example the magnetoelectric effect [1]). Accordingly, this approach is very promising to reveal unexpected phenomena. This leaves the question: Which materials shall be used?
For the propagation of spin-waves the material of choice is yttrium iron garnet (YIG), a ferromagnetic insulator with an unmatched low Gilbert damping of down to $\alpha = 5 \times 10^{-5}$ which for microwave frequencies only weakly depends on the excitation frequency [2, p.29]. This allows for a extremely narrow ferromagnetic resonance line width of 0.3 Oe for an excitation frequency of 9 GHz. Due to these high quality ferromagnetic resonances YIG is an interesting material for the investigation of spin-waves and the technical application in microwave generators.
For the emerging field of magnonics another consequence is interesting. In magnonics the large variety of phenomena connected to the excitation of spin-waves is used to transmit and process information. The transmission of information can be separated in four steps: Emission, transport, manipulation and detection of signals [3]. For the transport the decay length of spin-waves is of highest interest to efficiently transmit signals from the point of excitation to the point of detection. The low damping parameter of YIG enables for a spin-wave propagation length that can reach macroscopic distances making YIG a highly interesting material for magnonic devices.
The most promising candidate for electronics is graphene. Since its first successful preparation in 2004 [4] it is probably the most discussed material in physics during the last decade. The importance of this discovery can already be seen in more than 17,000 citations of the above mentioned publication and the Nobel prize in physics in 2010. Due to its many remarkable properties like electric and thermal conductivity, its mechanical stability and due to its thickness of a single layer of carbon atoms, graphene is a highly promising material for future developments. Although experiments still do not reach many of the theoretical predictions numerous exciting discoveries were made in the past years like for example the anomalous quantum-Hall-effect [5].
Since combining YIG for example with platinum has already lead to interesting

discoveries like the spin-Seebeck effect [6][7] a combination of YIG with such an multifaceted material as graphene is very promising.
The approach used in this thesis to examine YIG/graphene bilayers is to excite spin-waves in the YIG layer and detect a voltage in the graphene layer. The appearing voltage is closely examined for different spin-wave excitation powers, frequencies, orientations and magnitudes of the static magnetic field and the direction of the measured voltage with respect to the direction of spin-wave propagation. We will see that this voltage for some configurations can be explained by known phenomena. Other configurations enable for unexpected properties that - to our best of knowledge - cannot be explained by an existing theory so far, and a new model has to be developed.

2 Fundamental concepts

2.1 Magnetism

A magnetic field can induce different responses in different types of media. For a *diamagnet* the magnetic field excites electric currents leading to a magnetic moment and field with opposite orientation to the external field. In a *paramagnet* on the other hand magnetic dipole moments $\vec{\mu}$ are already present, but randomly oriented in space so the average magnetic moment is zero. Due to minimization of the *Zeeman energy*

$$E_{\mathrm{Z}} = -\vec{\mu} \cdot \vec{H} \tag{2.1}$$

an external magnetic field $\vec{H}$ leads to an alignment along the direction of the magnetic field [8, p. 70]. These intrinsic magnetic moments originate in the total angular momentum $\hbar\vec{J}$ of the electrons in the paramagnet and are given by

$$\vec{\mu} = -\gamma\hbar\vec{J} \tag{2.2}$$

where γ is the gyromagnetic ratio [9, p. 332]. Due to the negative charge of the electron the magnetic moment and the angular momentum are antiparallel. The total angular momentum is a sum of the orbital angular momentum $\hbar\vec{L}$ and the spin $\hbar\vec{S}$.
A special case of paramagnetism is the *ferromagnet*. Here the electron spins are strongly coupled by the *exchange interaction* leading to a net magnetic moment even for vanishing bias field [10, p. 208]. The nature of this interaction is the topic of the following section.

2.1.1 Exchange interaction

The origin of the exchange interaction can be found in a combination of Pauli's exclusion principle and the Coulomb interaction. In quantum mechachics the relative orientation of two electron spins cannot be changed without simultaneously transforming the spatial wave function due to Pauli's principle. This leads to changes in the Coulomb interaction and, hence, in the total energy of the system [2, p. 7]. Accordingly, the exchange interaction is a purely quantum mechanical effect without a classical analogue. A first model was proposed by Heisenberg in 1928 [11]. The

corresponding Hamiltonian is

$$H_{\text{ex}} = -\sum_i \sum_\delta J_{i\delta} \vec{S}_i \vec{S}_\delta \tag{2.3}$$

where $\vec{S}$ is the spin operator, the index δ determines the closest neighbours of the electron i and $J_{i\delta}$ is the *exchange integral* for two electrons [10, p. 208]. For increasing distance between the electrons the exchange integral quickly decreases so the exchange interaction is limited to short distances [2, p. 7]. Typically equation (2.3) is simplified by replacing the integral with the *exchange constant* J. For a ferromagnet J is positive and therefore a parallel alignment of the electron spins is preferred leading to a net magnetic moment. While the model's applications on transition metals are limited it is a good approximation for ferromagnetism with localized electrons [10, p. 198].

2.1.2 Magnetization

Due to the strong coupling between the electrons the magnetic moments - on a macroscopic scale - can behave like a single magnetic dipole. For quantification the *magnetization* $\vec{M}$ is defined as the density of magnetic moments

$$\vec{M} = \frac{1}{V} \sum_i^N \vec{\mu}_i \tag{2.4}$$

with N as the number of magnetic moments $\vec{\mu}_i$ within the volume V [2, p. 9]. If all magnetic moments are parallel the magnetization reaches its maximum value - the *saturation magnetization*. Since the magnetization is connected to the angular momentum of the electrons (see equation (2.2)) the orientation can be influenced by exerting torques leading a dynamic response of the magnetization. This introduces many physical phenomena. A basic overview will be given in the next section.

2.2 Dynamic magnetization theory

For a single magnetic dipole moment $\vec{\mu}$ a magnetic field $\vec{H}$ creates a torque $\vec{\tau}$ on the orientation of the dipole [8, p. 84]:

$$\vec{\tau} = \frac{d\vec{\mu}}{dt} = \vec{\mu} \times \vec{H}. \tag{2.5}$$

This can be used to describe the dynamic response of a ferromagnet to an applied magnetic field. If we return to a continuum approach using the magnetization we get the *Landau-Lifshitz-Gilbert equation* (LLG) which is the fundamental equation

of motion for the description of dynamic magnetic phenomena on a macroscopic scale:

$$\frac{d\vec{M}}{dt} = -\gamma\vec{M} \times \vec{H} + \alpha\frac{\vec{M}}{M} \times \frac{d\vec{M}}{dt}, \tag{2.6}$$

where α is the damping parameter [2, p. 17]. For vanishing damping the equation reduces to the *Landau-Lifshitz equation* [12] that can be derived by a combination of the equations (2.2), (2.4) and (2.5). The right hand side then reduces to $-\gamma\vec{M} \times \vec{H}$ which is always oriented perpendicular to the direction of the magnetization vector and the magnetic field. It therefore enforces a right-hand precession of the magnetization around the magnetic field. For an infinite, isotropic ferromagnet the precession frequency is the *Larmor frequency* [8, p. 85] that is given by

$$\omega_{\mathrm{H}} = \gamma H. \tag{2.7}$$

For non-vanishing α the second term in LLG is a phenomenological term to describe damping. It creates a torque towards the axis of precession and therefore reduces the opening angle that is a measure for the intensity of the excitation [13][14]. This movement is illustrated in figure 2.1.
In our current model we only used an external static magnetic field. In reality this is typically not the case. For a more flexible description the magnetic field $\vec{H}$ in equation (2.6) has to be replaced by an effective field $\vec{H}_{\mathrm{eff}}$. This field is calculated using the derivative of the free energy volume density F with respect to the magnetization [2, p. 32]:

$$\vec{H}_{\mathrm{eff}} = -\frac{\delta F(\vec{M})}{\delta\vec{M}}. \tag{2.8}$$

δ marks the functional derivative [14]. For an external field $\vec{H}_{\mathrm{ext}}$ the density of the free energy is given by the Zeeman energy:

$$F_{\mathrm{Zeeman}} = -\vec{M}\vec{H}_{\mathrm{ext}}. \tag{2.9}$$

The effective field then equals the external magnetic field as expected [2, p. 34]. Further contributions can be the exchange, the dipole-dipole or the anisotropy energy [2, p. 33].

2.2.1 Ferromagnetic resonance

A very interesting case is the combination of a static magnetic field $\vec{H}_0$ aligned along the z-axis and a dynamic field $\vec{h}$ in the xy-plane. In the simplest case both fields are homogeneous. If we postulate the dynamic field to be small compared to the

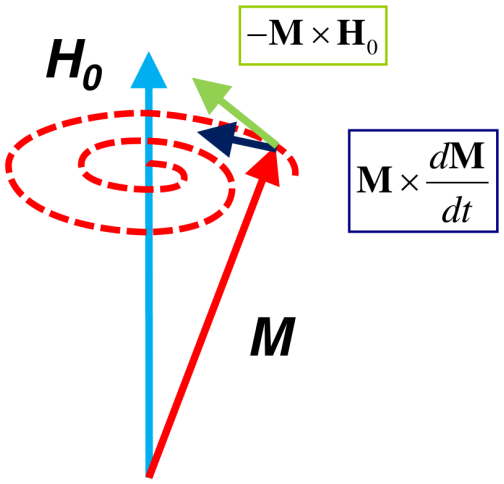

Fig. 2.1: Precession of the magnetization around the external magnetic field under the influence of damping [15].

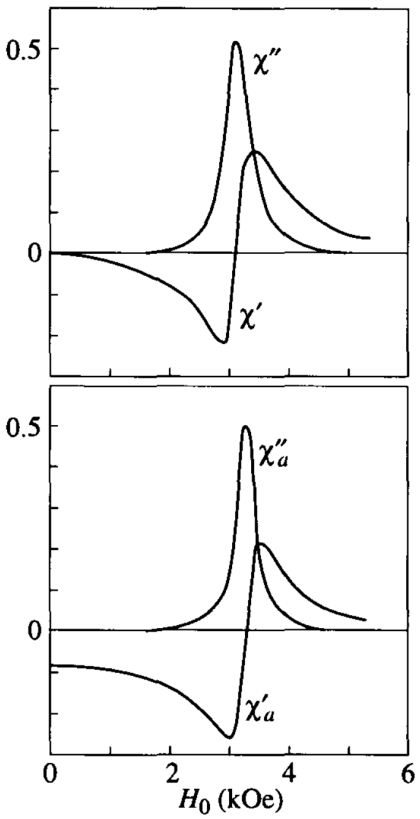

Fig. 2.2: Real and imaginary part of the components of the susceptibility tensor $\overleftrightarrow{\chi}$ for M_0=160 G, α = 0.025 and f = 9.4 GHz in dependence of the static magnetic field [2, p. 20].

static field it is plausible that a similar assumption can be done for the dynamic part of the magnetization. Accordingly, the total magnetization can be separated in a static part $\vec{M}_0$ that equals the saturation magnetization oriented along the static magnetic field and a dynamic part $\vec{m}$ [2, p. 10]:

$$\vec{H} = \vec{H}_0 + \vec{h} \tag{2.10}$$

and

$$\vec{M} = \vec{M}_0 + \vec{m}. \tag{2.11}$$

In this case we can derive a linear relation between the dynamic magnetic field and the dynamic magnetization

$$\vec{m} = \overleftrightarrow{\chi} \cdot \vec{h} \tag{2.12}$$

$$\Rightarrow \begin{pmatrix} m_\mathrm{x} \\ m_\mathrm{y} \\ m_\mathrm{z} \end{pmatrix} = \begin{pmatrix} \chi & \mathrm{i}\chi_\mathrm{a} & 0 \\ -\mathrm{i}\chi_\mathrm{a} & \chi & 0 \\ 0 & 0 & \chi_\parallel \end{pmatrix} \cdot \begin{pmatrix} h_\mathrm{x} \\ h_\mathrm{y} \\ h_\mathrm{z} \end{pmatrix}. \tag{2.13}$$

$\overleftrightarrow{\chi}$ is the dynamic susceptibility which is a dimensionless, second-order tensor [2, pp. 11]. Its components χ and χ_a are complex functions of the static magnetic field H and the excitations frequency ω_H. For vanishing damping they are given by

$$\chi = \frac{\gamma M_0 H_0}{H_0^2 - (\omega_\mathrm{H}/\gamma)^2} \tag{2.14}$$

$$\chi_\mathrm{a} = \frac{M_0 \omega_\mathrm{H}}{H_0^2 - (\omega_\mathrm{H}/\gamma)^2}. \tag{2.15}$$

We see that both components show a resonant behaviour for $\gamma H_0 = \omega_\mathrm{H}$ [2, p. 12]. In a real physical system the damping is not zero and the divergence at these points vanishes. χ and χ_a then get far more complex and can be separated in a real and an imaginary part:

$$\chi = \chi' + \mathrm{i}\chi'' \tag{2.16}$$

$$\chi_\mathrm{a} = \chi'_\mathrm{a} + \mathrm{i}\chi''_\mathrm{a}. \tag{2.17}$$

In experiments typically the absorption of electromagnetic energy is detected which is connected to the imaginary parts χ'' and χ''_a [2, p.17]. For a properly chosen frequency and static magnetic field the tensor components χ and χ_a show a resonant behaviour as can be seen in figure 2.2. This phenomenon is called *ferromagnetic resonance*. The magnetic resonance field will in the following be referred to as FMR-field.
The component $\chi_\parallel$ in general is very small and vanishes for $\alpha = 0$. In this case no dynamic magnetization is excited in the z-direction.

The demagnetizing field

In the previous sections we only regarded bulk ferromagnets. For a finite structure we always have to consider the creation of "magnetic charges" at the surface of a ferromagnet caused by uncompensated magnetic moments (see fig. 2.3). This leads to the so called *demagnetizing field* that reduces the internal magnetic field [8, pp.49] and can be included into LLG via equation (2.8). The calculation can be

realized via the *demagnetization tensor* $\overleftrightarrow{N}$ that depends on the sample shape and the magnetocrystalline anisotropy. It is a second-order tensor with its trace equal to 4π [16]:

$$\vec{H}_{\text{int}} = \vec{H}_{\text{ext}} - \overleftrightarrow{N}\vec{M}. \tag{2.18}$$

The tensor becomes diagonal for an isotropic, ferromagnetic ellipsoid with its principal axis along the x-,y- and z-axis [17]. In this simplified case there are only three independent components $N_{\text{x}}, N_{\text{y}}$ and N_{z}. If we calculate the resonance frequency ω_{H} for $\alpha = 0$ and the static magnetic field applied along the z-axis we get the Kittel equation:

$$\omega_{\text{H}} = \gamma\sqrt{[H_0 + (N_{\text{y}} - N_{\text{z}})M_z] \cdot [H_0 + (N_{\text{x}} - N_{\text{z}})M_z]}. \tag{2.19}$$

In this case the resonance frequency no longer solely depends on the static magnetic field but also on the magnetization along the z-axis that is typically equal or close to the saturation magnetization M_0. For this thesis we only need the case of a plane infinite ellipsoid (see fig. 2.4) that is magnetized (i) in-plane or (ii) out-of-plane:

$$\text{(i)} \quad \omega_{\text{H}} = \gamma\sqrt{H_0(H_0 + 4\pi M_0)} \quad | \; N_{\text{x}} = N_{\text{z}} = 0; \; N_{\text{x}} = 4\pi \tag{2.20}$$

$$\text{(ii)} \quad \omega_{\text{H}} = \gamma(H_0 - 4\pi M_0) \quad | \; N_{\text{x}} = N_{\text{y}} = 0; \; N_{\text{z}} = 4\pi \tag{2.21}$$

We can see from these equations that the precession frequency and therefore the energy in the first geometry is increased due to dynamic magnetic charges at the ellipsoid surface leading to additional dynamic fields [15]. The corresponding fields also change the movement of the magnetization and enforce an elliptic precession. For out-of-plane magnetized films the internal static magnetic field is reduced without creating additional dynamic fields. In this case the energy is simply shifted to lower values but shows the same slope as it does for a ferromagnetic bulk.

2.2.2 Spin-waves

In the previous sections we analysed the dynamics of the magnetic system in homogeneous fields. The situation changes if we apply a local dynamic field. In this case the resonance is only excited locally. This disturbance can propagate as a wave through the ferromagnet since neighbour spins are no longer aligned parallel to each other (see fig. 2.5). These deviations of the angle lead to dynamic energy terms caused by the exchange and the dipolar interaction. According to equation (2.8) both terms create additional dynamic magnetic fields exerting torques on the magnetization. Under the assumption that no alternating electric fields and electric currents exist in the system (magnetostatic approximation [2, p. 147]) the Maxwell

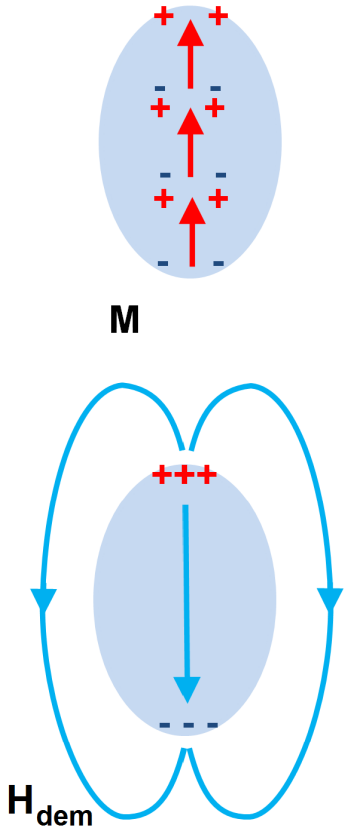

Fig. 2.3: Uncompensated magnetic moments creating "magnetic charges" at the surface of a ferromagnet [15].

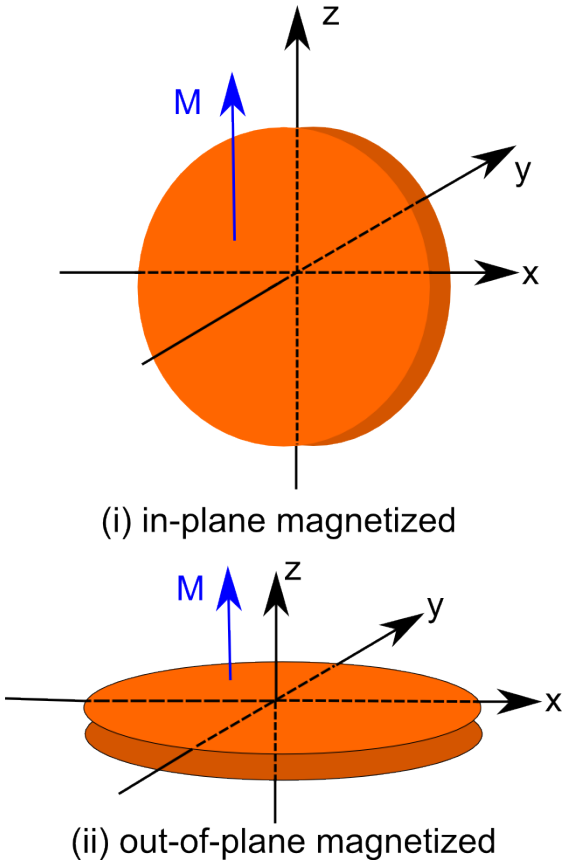

Fig. 2.4: Infinite plane ellipsoid magnetized (i) in-plane and (ii) out-of-plane.

equations reduce to

$$\nabla \cdot \vec{b} = 0, \qquad \nabla \times \vec{h} = 0. \tag{2.22}$$

In this case the dispersion relation of the wave away from the point of excitation is only determined by the static magnetic field and the two dynamic magnetic fields that can be calculated. For simplification we start with an isotropic, ferromagnetic bulk. If we assume the propagating spin-wave to be a plane wave with wave vector $\vec{k}$ we have

$$\vec{m}(\vec{r}) = \vec{m}_0 \mathrm{e}^{i(\omega t - \vec{k}\vec{r})}. \tag{2.23}$$

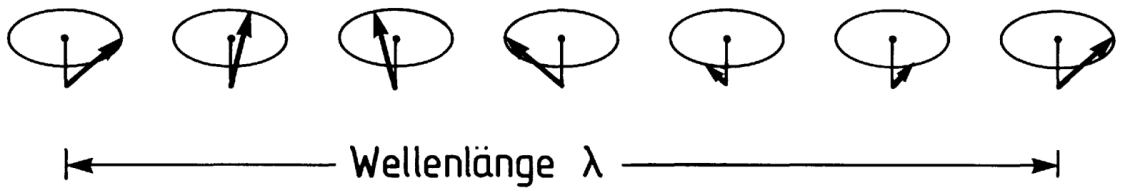

Fig. 2.5: Spin-wave with wavelength λ [10, p. 216].

Using equation (2.22) and (2.23) we can determine the dynamic dipolar interaction:

$$\vec{h}_{\mathrm{d}} = -\frac{4\pi}{|\vec{k}|^2}\vec{k}\cdot\left(\vec{k}\cdot\vec{m}\right). \tag{2.24}$$

The equation shows that the dipolar field does not depend on the magnitude of the wave vector but on the angle between the direction of propagation $\vec{k}$ and the dynamic magnetization $\vec{m}$ and is therefore anisotropic [18]. In the case of perpendicular orientation of $\vec{m}$ relative to $\vec{k}$ the dipolar interaction between neighbouring spins vanishes. Since the dynamic magnetization is perpendicular to the static magnetic field this case corresponds to the propagation of spin-waves in the direction of the static magnetic field.
For the dynamic exchange field we see a different behaviour. The exchange interaction in equation (2.3) can be separated in a uniform term and a component that describes the non-uniformity of the orientation of the spins [2, p.179]. For an isotropic ferromagnet this non-uniform component can be simplified to

$$\vec{h}_{\mathrm{ex}} = -q\nabla^2\vec{m} \tag{2.25}$$

with q as the exchange stiffness. If we take a look at a plane wave we get

$$\vec{h}_{\mathrm{ex}} = q\vec{k}^2\vec{m}. \tag{2.26}$$

We see that the exchange energy does not depend on the orientation of the wave vector but on its magnitude and is therefore isotropic.

Influence of the sample shape

As we have seen in section 2.2.1 the finite sample shape and the magnetic dipole moments create magnetic charges at the surface. This leads to additional magnetic fields that influence the energy of the magnetic system. In the dynamic case these fields depend on the magnitude of the wave vector and its angle to the static magnetic field. In an out-of-plane magnetized film the angle between the static magnetic

field and the in-plane wave vector k is always 90° and is therefore independent of the orientation of k. The corresponding waves are called *forward volume magnetostatic waves* (FVMSW). The dispersion relation is shown in figure 2.6a.
For in-plane magnetized films the situation gets more complicated. For an angle of 90° between H_0 and k *magnetostatic surface waves* (MSSW) also called *Damon-Eshbach modes* [19] are excited that propagate on one of the surfaces and the amplitude decays exponentially with increasing distance from the surface.
More important for this thesis is the excitation of *backward volume magnetostatic waves* (BVMSW) that appear for a vanishing angle between the in-plane wave vector and the static magnetic field. The dispersion relation is shown in figure 2.6b. The plot reveals that the group velocity defined by

$$\vec{v}_{\mathrm{gr}} = \frac{\partial \omega}{\partial \vec{k}} \tag{2.27}$$

is always negative. This means that the energy transport for BVMSWs points in the opposite direction than the wave vector which is the origin of the name.
In both cases the spectrum depends on the static magnetic field. For increasing magnetic field the spectra are shifted to higher frequencies while the group velocity for a given wave vector only changes slightly. For a fixed excitation frequency we then observe resonance conditions for different k-vectors when the magnetic field is varied.

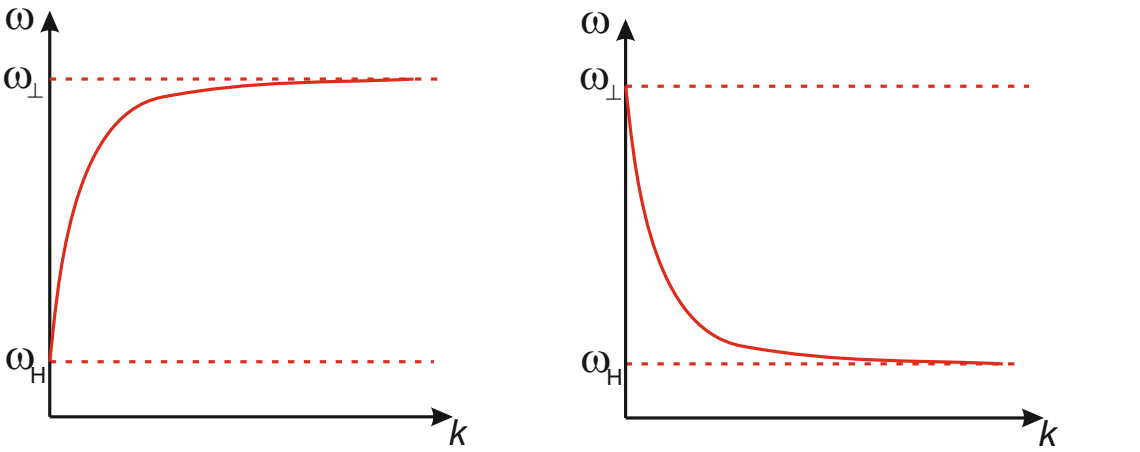

(a) Forward volume magnetostatic waves (FVMSW).

(b) Backward volume magnetostatic waves (BVMSW).

Fig. 2.6: Dispersion relation where ω_{H} is the Larmor frequency (see equation (2.7)) and $\omega_{\perp}$ is the resonance frequency for in-plane magnetized films (see equation (2.21)) [15].

2.3 Magnetoelectric effect

2.3.1 Thermodynamic considerations

The *magnetoelectric effect* (ME effect) is the induction of a polarization by a magnetic field or the creation of a magnetization as response to an electric field. For a better understanding we have to take a look at an expansion of the free energy volume density F with respect to the components of the applied magnetic fields $\vec{H}$ and electric fields $\vec{E}$ [20][1]. Using Einstein's summation convention we have

$$F(\vec{E},\vec{H}) = F_0 \underbrace{-M_i^{\mathrm{S}} H_i}_{\mathrm{I}} \underbrace{-P_i^{\mathrm{S}} E_i}_{\mathrm{II}} \underbrace{-\frac{1}{2}\frac{\mu_{ij} H_j H_i}{4\pi}}_{\mathrm{III}} \underbrace{-\frac{1}{2}\frac{\varepsilon_{ij} E_j E_i}{4\pi}}_{\mathrm{IV}} \underbrace{-\alpha_{ij} E_i H_j}_{\mathrm{V}} + \dots \tag{2.28}$$

F_0 marks the energy part that is independent of the electric or magnetic field. Term I and III determine the Zeeman-energy for (I) the spontaneous magnetization $\vec{M}^{\mathrm{S}}$ and (III) the induced magnetization where μ_{ij} are the components of the magnetic permeability tensor ($\mu_{ij} = \delta_{ij} + 4\pi\chi_{ij}^{\mathrm{m}}$ with χ_{ij}^{m} as the magnetic susceptibility [21, p. 106]). Similarly, term II determines the free energy density of the spontaneous polarization $\vec{P}_i^{\mathrm{S}}$ in an electric field. The polarization is the electric analogue to the magnetization and is a measure of the density of electric dipole moments [22, p. 142]. Accordingly, term IV is the energy of an induced polarization in an electric field with ε_{ij} as the components of the electric permittivity tensor ($\varepsilon_{ij} = \delta_{ij} + 4\pi\chi_{ij}^{\mathrm{e}}$ with χ_{ij}^{e} as the electric susceptibility [21, p. 36]). These first terms follow basic principles. Term V is as well as the induction terms a second order contribution to the free energy, but is a mixed term of the electric and magnetic field. The unsymmetrical second order tensor α_{ij} is the *magnetoelectric susceptibility tensor*. Since both fields only contribute linearly to this term α_{ij} determines the *linear magnetoelectric effect*. Similarly to equation (2.8) the magnetization can be calculated by differentiation of equation (2.28) with respect to the magnetic field [20][1]:

$$M_i(\vec{E},\vec{H}) = -\frac{\partial F(\vec{E},\vec{H})}{\partial H_i} \tag{2.29}$$

$$= M_i^{\mathrm{S}} + \chi_{ij}^{\mathrm{m}} H_j + \alpha_{ji} E_j. \tag{2.30}$$

We see that due to the magnetoelectric effect an electric field can lead to a magnetization. In an equivalent way a magnetic field can create a polarization:

$$P_i(\vec{E},\vec{H}) = -\frac{\partial F(\vec{E},\vec{H})}{\partial E_i} \tag{2.31}$$

$$= P_i^{\mathrm{S}} + \chi_{ij}^{\mathrm{e}} E_j + \alpha_{ij} H_j. \tag{2.32}$$

Experiments show that for compounds the ME response is typically rather low since the components of the magnetoelectric susceptibility are limited by the electric and magnetic susceptibilities due to thermodynamic stability [23]:

$$\alpha_{ij}^2 \ < \ \chi_{ij}^{\mathrm{e}} \chi_{ij}^{\mathrm{m}}. \tag{2.33}$$

Since both the electric and ferromagnetic susceptibility strongly depend on the temperature the ME susceptibility is affected as well. Additionally only materials with ferromagnetic, ferroelectric or multiferroic properties show relevant contributions. For most compounds this is not the case. Only a few materials (including garnet films) reach higher values. For garnet films the orientation of the magnetization changes when an electric field is applied since the magneto-crystalline anisotropy is affected [24]. Still, even for larger values only about 1 of 10^5 spins changes its orientation [1]. A way to increase the ME response will be shown in section 2.3.3.

2.3.2 Symmetry considerations

Symmetry considerations show that the linear magnetoelectric effect can only be observed for materials with broken time reversal and spatial inversion symmetry [1]. Magnetic fields and the magnetization are connected to the angular momentum of electrons and are accordingly not invariant under time reversal but stay unchanged under spatial inversion:

$$\vec{H} = -\hat{T}\vec{H} \qquad \text{and} \qquad \vec{H} = \hat{I}\vec{H} \tag{2.34}$$

where $\hat{T}$ is the time-reversal operator and $\hat{I}$ is the spatial inversion operator. For electric fields and the polarization we have the opposite case. The spatial inversion symmetry is broken while time reversal leaves the system unchanged.

$$\vec{E} = \hat{T}\vec{E} \qquad \text{and} \qquad \vec{E} = -\hat{I}\vec{E} \tag{2.35}$$

If we assume for the free energy to be constant it does not vary under time reversal and spatial inversion. For the first four terms in equation 2.28 this symmetry is automatically fulfilled. For the linear ME effect it is necessary that the time reversal and spatial inversion symmetry are broken at the same time:

$$\begin{aligned} F_{\mathrm{ME}} &= \hat{I} F_{\mathrm{ME}} \\ &= -\hat{I}(\alpha_{ij} E_i) \cdot H_j \\ &= -(-\alpha_{ij}) \cdot (-E_i) \cdot H_j \\ &= -\alpha_{ij} E_i H_j = F_{\mathrm{ME}} \end{aligned} \qquad \begin{aligned} F_{\mathrm{ME}} &= \hat{T} F_{\mathrm{ME}} \\ &= -\hat{T}(\alpha_{ij} H_j) \cdot E_i \\ &= -(-\alpha_{ij}) \cdot (-H_j) \cdot E_i \\ &= -\alpha_{ij} E_i H_j = F_{\mathrm{ME}}. \end{aligned} \tag{2.36}$$

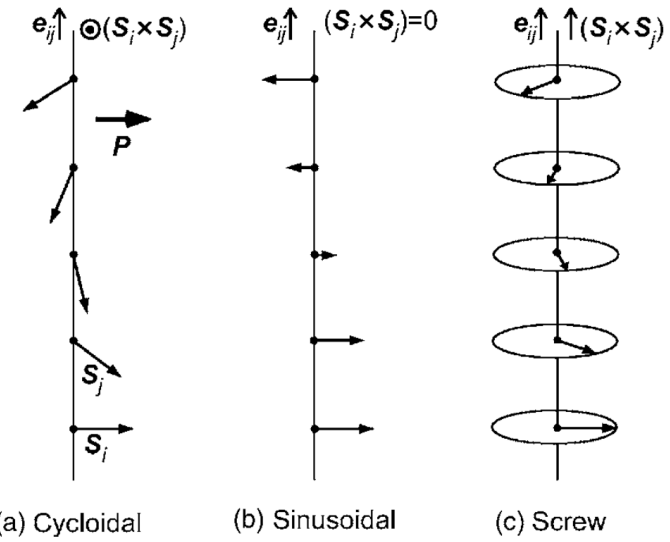

Fig. 2.7: a) Cycloidal, b) sinusoidal and c) screw spin-ordering [26].

A simple approach to time-inversion violation is a material with spin-ordering - for example a ferromagnet. If the spin-ordering also breaks the inversion symmetry magnetoelectric coupling appears. An examples would be a toroidal [25] or a cycloidal order of spins while the very similar screw or a sinusodial spin-order do not fulfil this requirement [26] (see fig. 2.7).

2.3.3 Laminated composits

In section 2.3.1 we saw that for compounds the ME effect is not strongly pronounced. An improvement can be reached for layered composites of piezoelectric and magnetostrictive compounds. Here, mechanical stresses mediate between the electric and magnetic fields [27]. Due to the complex interaction between the constituents the relation between the applied field and the response field is typically non-linear. Still, a linear response can be achieved using a large bias field and a small ac-probing field [1]. In this case the ME effect can show strong dependence on the frequency of the ac-field. Resonances can be observed for frequencies matching magnetic, electric or mechanical eigenmodes depending on the shape and properties of the analysed structure [28].
For the piezo layer typically $PbZr_{1-x}Ti_xO_3$ (PZT) is used, because it is commercially available [1]. As a magnetostrictive compound many materials were tested including garnets [29]. For laminated composites the ME response is affected by four aspects:

- *Material parameters* influence the strength of the piezoelectric and magnetostrictive effects and therefore the ME response.

- *Stacking parameters* like the thickness ratios of the magnetostrictive and piezoelectric layer t_m/t_p affect the overall behaviour. A thinner piezo layer leads to stronger tensions at the interface, but the voltage output reduces with increased t_m/t_p [1], so the effect is rather complex.

- *Bonding* at the interface determines the coupling of the mechanical stresses between the constituents.

- *Geometric aspects* describe the dependence on the orientation of the applied and detected fields. For the relative orientation of the bias fields one usually distinguishes the longitudinal (parallel alignment) and transverse (perpendicular orientation) ME effect. Experiments show that the transverse ME effect is larger then for the longitudinal case [30] [31]. For the orientation of the ac-probing field relative to the applied dc field a minimum can be observed for perpendicular orientation [27].

For experiments with laminated composites the measured effect for an applied magnetic field and detected electric field is usually characterized by the electric field [27]

$$E_i = \alpha_{ij}^{E} H_j \tag{2.37}$$

with

$$\alpha_{ij} = \varepsilon_{ik} \alpha_{kj}^{E}. \tag{2.38}$$

Typically a voltage and not an electric field is detected. If we assume the electric field to be homogenous across the distance d between the contacts for voltage measurements we have

$$V_i = d \cdot \alpha_{ij}^{E} H_j. \tag{2.39}$$

where V_i is the voltage caused by the i-th component of the electric field.

2.4 Graphene

2.4.1 Electronic properties

Graphene is an automatically thin material consisting of a monolayer of carbon atoms arranged in a hexagonal lattice also called *honeycomb lattice* (see fig. 2.8c). The sp^2-hybridisation of the carbon atoms creates completely 2-dimensional structures with a delocalized π-electron system [32]. This enables a very high electron mobility. The electronic structure leads to an intersection of the valence and conduction band at six points in phase space called *Dirac points* (see fig. 2.8a). Due to these intersection points graphene is a semiconducting material with vanishing band gap. The name of the Dirac points originates in the linear dispersion relation in both the conduction and valence band close to these points (see fig. 2.8a). Accordingly, electrons with energies close to the point of intersection behave like massless Dirac fermions moving at an energy independent velocity of about 1/300-th the speed of light [33].
A closer examination reveals that only two Dirac points are independent. This provides a fascinating property. Since an electron can have the same energy and wave vector but can be found in either of these Dirac cones these two possible electron states create a new degree of freedom - the so called *pseudospin* [33].

Manipulation of the Fermi level

While the electron mobility in graphene is very high the density of states converges to zero at the Dirac points leading to a maximum resistivity. Accordingly, the conductivity of graphene strongly depends on the position of the Fermi level relative to the Dirac points. This energy difference can be influenced by doping graphene. While p-doping - for example due to crystallographic defects - leads to a shift to energies below the Dirac point n-doping causes the opposite behaviour (see fig. 2.8b). Due to the strong influence on the conductivity the energy shift of the Dirac point to the Fermi level can be measured and used as an indicator for the quality of the produced graphene samples by applying a gate voltage and simultaneously measuring the conductivity [34].
But not only doping can influence the electronic properties of graphene. The electronic structure of graphene does not allow for out-of-plane covariant bondings. Accordingly graphene layers are only weakly coupled via van der Waals interactions to a given substrate. Measurements show that the interaction energy for graphene and for example SiO2 is given by $0.45\,\mathrm{J/m^2}$ [35] while it reaches $0.72\,\mathrm{J/m^2}$ for metals like copper [36]. Although this interaction is very weak and mostly leaves the π-orbitals intact properties like the electron mobility are very sensitive to the roughness and other properties of the substrate surface. Depending on the substrate material, the

production technique and the temperature the electron mobility can vary by several orders of magnitude [33].
Additionally voltage and current measurements in graphene are very sensitive to the contacts used on graphene. Depending on the material and the contact thickness the contacts can even locally dope the graphene layers beneath the contacts area [37]. Experiments show that the best results can be reached using gold due to its noble properties and high conductivity [33].

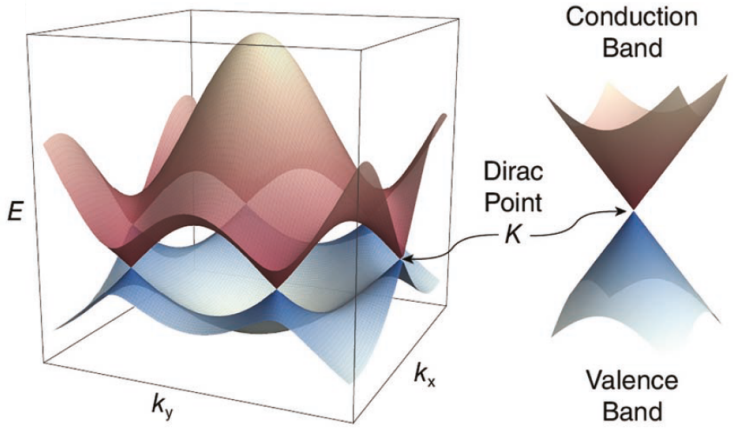

(a) Dispersion relation of graphene showing the characteristic vanishing band gap at the Dirac points [33].

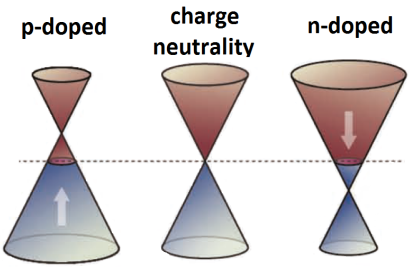

(b) Influence of doping on the Fermi level in graphene [33].

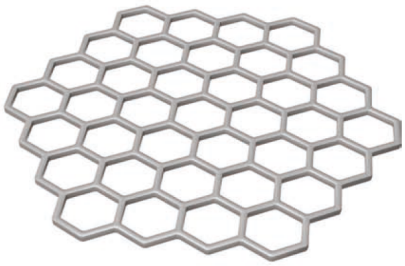

(c) Hexagonal two dimensional lattice structure of graphene [33].

Fig. 2.8: Properties of graphene.

2.4.2 Magnetic properties

At room temperature graphene is found to be strongly diamagnetic for out-of-plane magnetized structures [38]. The in-plane diamagnetic susceptibility reduced by two orders of magntiude [38]. For temperatures above 50 K the paramagnetic background is negligible [39]. For lower temperatures the contribution of paramagnetism

can be observed independent of the orientation of the magnetic field relative to the graphene layer. After subtraction of the diamagnetic component it perfectly matches the standard Brillouin function [38]. Measurements on samples under the influence of radiation reveal the origin of the magnetic moments to be found in vacancies with spin 1/2. These magnetic moments are uncoupled and do not allow for ferromagnetism even at temperatures of 2 K and vacancy concentrations close to the instability of the used graphene samples [39].

3 Experimental methods

3.1 Bilayers

In our experiments we used two different yttrium iron garnet ($Y_3Fe_5O_{12}$)/graphene bilayers (see fig. 3.1). The YIG layer of both bilayers has a thickness of 5.1 µm and is grown on Gadolynium-Gallium-Garnet (GGG) by *liquid phase epitaxy* [40][41]. Both YIG layers are part of the same YIG sample cut into smaller pieces.
The graphene layers were produced by the research group of August Yurgens[1]. Two different methods were used. The first layer was grown on copper by *low partial pressure chemical vapor depostion* [34]. To separate the copper and graphene layers electrolysis of water was used. The creation of H_2 bubbles quickly detaches the graphene layer that can be transferred to a new substrate using a spin coated poly(methyl methacrylat) frame. This method produces high quality monolayers of graphene leaving the copper catalysator unharmed [42]. After separation the graphene layer is placed on the YIG film.
The second sample is created in a very similar way. In this case the graphene layer is grown on platinum. Due to fine tuning of the growth parameters high quality monolayers of graphene can be produced [43].
In both samples the Fermi level is found to be close to the Dirac point indicating a negligible number of defects. For simplicity the used samples will be referred to as the Pt-grown and the Cu-grown sample.
To be able to measure voltages in the graphene layer ten gold contacts are placed on top of the structures. The longitudinal distance between the centre of the contacts A and B as well as C and D is 1.30 mm. The transversal distance (distance between A and C or B and D) is 1.20 mm. The contacts are quadratic with a side length of 0.5 mm.
Additionally two YIG-aluminium bilayers with a similar gold-contact structure were created for reference measurements. The YIG layers were grown by liquid phase epitaxy and have a thickness of 6 µm. The aluminium layers were again created by the research group of August Yurgens using a *physical vapor deposition by evaporation* method [44]. The thickness of both aluminium layers is 6 nm.

[1] Quantum Device Physics Laboratory Department of Microtechnology and Nanoscience Chalmers University of Technology, Göteborg, Sweden

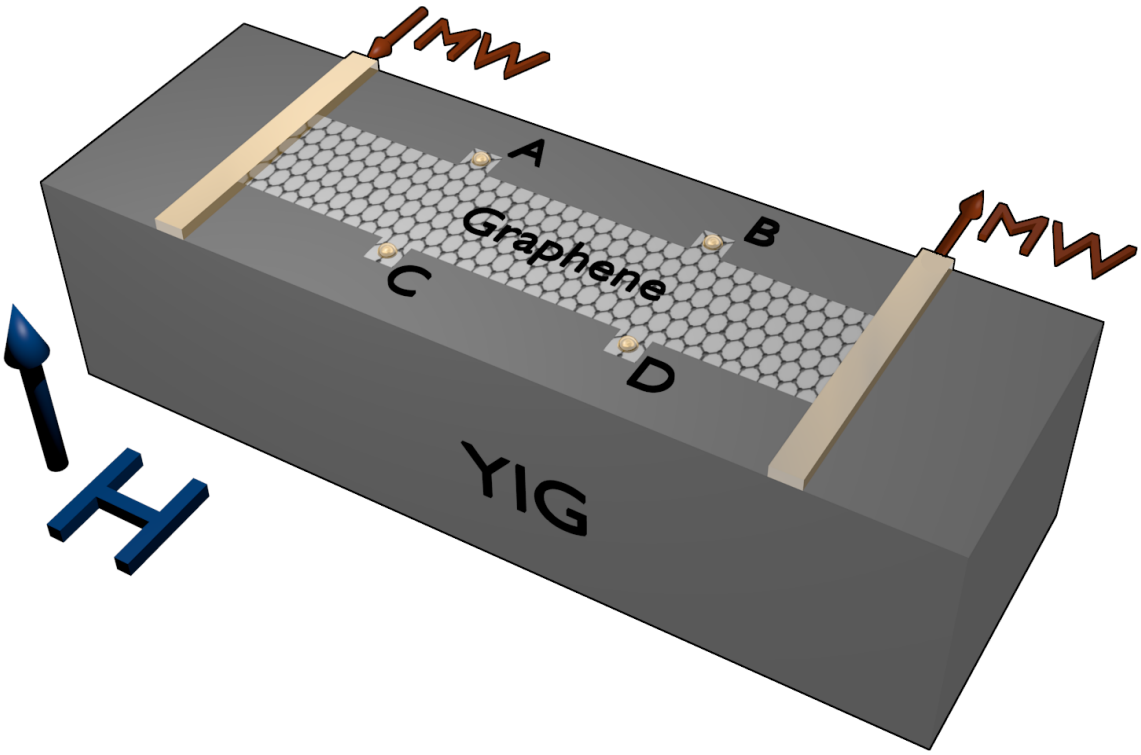

Fig. 3.1: YIG/graphene bilayer with four gold contacts for voltage measurements between two microwave antennas [45].

3.2 Experimental Setup

In our experiments we use a microwave spectroscopy setup to excite and analyze spin-waves in the YIG layer. This setup is combined with a lock-in technique to be able to measure the voltage in the graphene layer [46] (see fig. 3.2). A list of used devices can be found in table 3.1.

To be able to flexibly create and control the static magnetic field an electromagnet connected to a current source is used. The calibration is shown in appendix A.2. The dynamic magnetic field is created using a microwave generator. The microwave signal is injected into a stripline antenna with a width of 50 µm and 50 Ω wave resistance. The ac-current within the stripline creates (in first approximation) a linearly polarized magnetic field within the ferromagnet parallel to the width of the stripline (see fig. 3.3). To avoid damages of the graphene layer the structures are placed on stripes of Sellotape.

The microwave signal is injected into the stripline through a directional coupler so that the reflected signal can be separated and measured using a microwave detector. The directional coupler attenuates the reflected signal by about 10 dBm. The exact value is frequency dependent and has to be calibrated (see appendix A.1.2). For

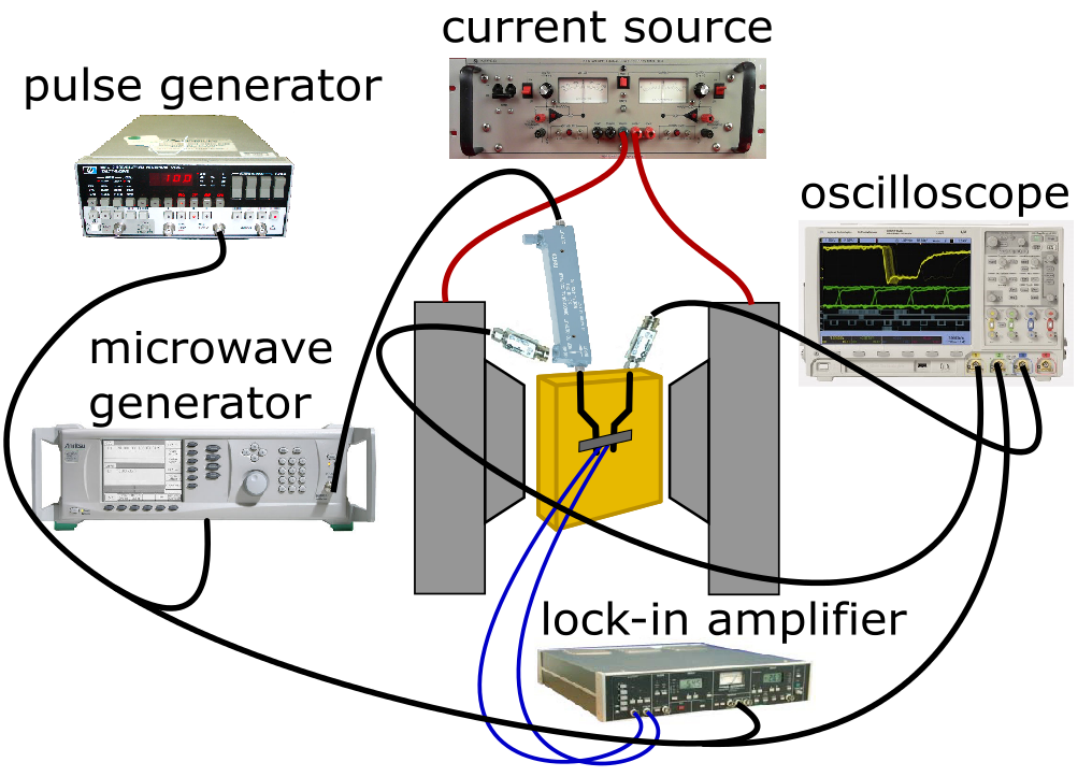

Fig. 3.2: Experimental setup.

static magnetic fields far away from the FMR-field the reflection has the constant value R_0. For magnetic fields that allow for the excitation of spin-waves the reflection signal reduces and is given by $R(H)$. The difference between the constant and reduced reflection is equal to the absorption of microwaves:

$$P(H) = R_0 - R(H). \tag{3.1}$$

The detection of the transmission signal is realized via a second microwave antenna. In contrast to the reflection the transmission is zero for magnetic fields far away from the FMR-field and increases for fields that allow for spin-wave excitation. The dynamic dipolar field of the spin-wave induces an ac-current with the same frequency and can be detected by a second microwave detector. The calibration of the two microwave detectors can be found in appendix A.1.1. To read out the received signals both microwave detectors are connected to an oscilloscope.
To be able to detect the low voltages appearing in graphene (µV scale) we use a lock-in technique. Therefore, we use a pulse-generator creating a rectangular pulse with a pulse repetition rate of 10 kHz. The original microwave signal and the pulse

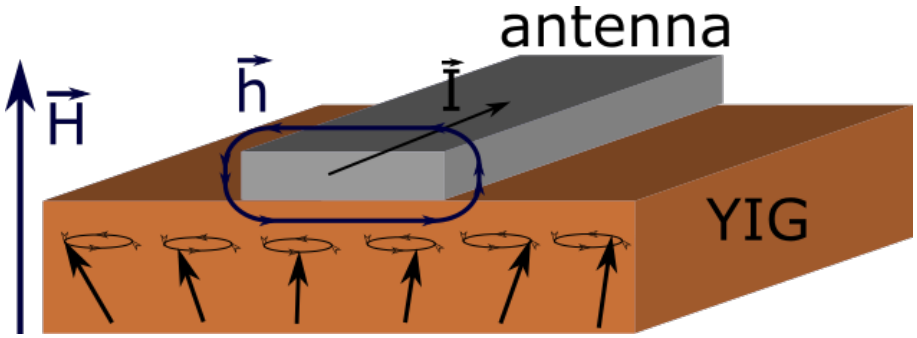

Fig. 3.3: Excitation of spin-waves using the linear polarized dynamic field of a stripline antenna.

are combined via a modulator integrated into the microwave generator so we get a pulsed excitation of spin-waves. The rectangular pulse is also the reference signal for the lock-in amplifier and the trigger for the oscilloscope. The lock-in amplifier is connected to the gold contacts at the graphene layer to measure the appearing voltage.
The current source, the microwave generator, the oscilloscope and the lock-in amplifier are connected to a computer to control and read-out the data of the experiment using a LabView program [47].

device	type
current source	Kepco-Bop M20-20
microwave generator	Anritsu - MG3692C Signal Generator 20GHz
pulse generator	HP 8116A Pulse/Function Generator 50MHz
oscilloscope	Agilent Technologies Infiniium DSO9064A 600MHz 10GSa/s
lock-in amplifier	AMETEK - Single Phase Lock-in Amplifier Model 5209

Tab. 3.1: Used devices and specific type.

During the measurements the excitation power and frequency are set to fixed values and the static magnetic field is changed in discrete steps by changing the electric current in the electromagnet. For every magnetic field the microwave reflection and

transmission as well as the lock-in voltage are measured. Usually an interval of 0.6 A (about 150 Oe) is divided in 300 steps. The 0.6 A are chosen since this is enough to detect approximately the entire absorption spectrum above the noise level. An increment of the number of steps would not lead to the gain of more relevant information, but would make measurements unnecessarily slow since every step takes about 3.5 seconds.
After every scan the orientation of the magnetic field is reversed and the scan is repeated. Typically for every orientation, excitation power and frequency the measurement scan is repeated 5 times to ensure reproducibility. Additionally this way the results can be averaged to reduce noise.
To avoid fluctuations of the temperature sensitive magnetization (see Bloch's $T^{3/2}$-law [10, p. 218]) and possible fluctuations of the graphene voltage the bilayer temperature is heated to 21.50±0.05°C. Since the chosen value does not strongly vary from room temperature it is not expected to strongly influence the measured values, but it is high enough to overcome fluctuations caused by the air conditioning.

3.3 Data analysis

Since our setup is automated it creates a large amount of data. A typical data file consist of four columns:

1. Electric current used to create the static magnetic field in Ampere
2. Reflection of microwaves in Volt
3. Transmission of microwaves in Volt
4. Graphene voltage in numbers between -10,000 and 10,000 given by the lock-in amplifier.

To be able to handle the analysis a C++-program was written using the Cygwin compiler [48] so that all the calculations on the collected data could be automated. The main analysis of this program runs through multiple stages:

1) Bad data files are eliminated: These files contain a voltage signal of zero in every step due to a communication error with the lock-in amplifier. Single events with a zero voltage during other measurements are also ignored for the same reason.

2) Calibration of the magnetic field (see appendix A.2).

3) Calibration of the microwave signals: The signals of the microwave detectors for reflection and transmission are calibrated with respect to the excitation frequency (see appendix A.1.1).

4) Attenuation correction: The reflected signal is attenuated by about 10 dBm. This attenuation is frequency dependent which will be considered in the correction (see point A.1.2).

5) Calibration of the lock-in voltage: The lock-in voltage is calibrated as described in the manual of the amplifier [49]. Actually, the manual is wrong by a factor of ten which has been accouted for in this program.

6) Offset Correction: The offsets of the microwave signals and the lock-in voltage are subtracted from the data. The offset is usually determined by taking ten points at both ends of the magnetic field interval where the resonance signal is close to zero.

7) Mean values and statistical uncertainties: If two or more files of the same frequency and excitation power were measured the program automatically starts calculating the mean values and statistical uncertainties for the microwave signals and the lock-in voltage. This is done in three steps:

   i) Peak shift: Since the position of the absorption signal with respect to the static magnetic field is not fixed in time - for example due to fluctuations of the environment temperature - all absorption signals will be shifted to the first file with the same settings using a χ^2-fit. Since the shift is only a few Oersted and we are not interested in the exact value of the magnetic field this is a legitimate method.

   ii) Comparing the magnetic fields: Every measured point of the first and the currently analyzed measurement will be compared with respect to the static magnetic field. If the magnetic fields match, the corresponding y-value (reflection, transmission or lock-in voltage) will be used for mean value calculations. If for a single magnetic field the mean value calculation uses a number of points lower than the number of files used for analysis it will be ignored for further calculations since these points are more sensitive to statistical fluctuations and might show confusing results. A lower number of points can be caused be excluded values due to a zero voltage (see point 1)) or due to points that are located at the end of the scanned interval and due to the peak shift do not match a magnetic field in the first measurement.

   iii) Statistical uncertainties: For every point used in the mean value calculation the statistical uncertainty Δx will we calculated using:

$$\Delta x = \tau \cdot \frac{\Delta s}{\sqrt{n}} \tag{3.2}$$

   where Δs is the unbiased sample variance, n the number of measurements and τ is the studentized variate [50, p. 76].

8) Log-Files: The program creates a log-file that collects information of every analyzed file like time passed since the beginning of the first measurement, the maximum values of the microwave signals and graphene voltage, the magnetization calculated from the maximum absorption or the offset values.

9) Origin-Scripts: As a bonus the program creates a file containing the commands to plot all this data using the program OriginPro 9.1 [51] that is used to create every plot in this thesis.

The program provides two further functions:

1) Peak shift: The peak shift described in point 7i) can be used for independent measurements and datasets. This way it is possible to compare measured values with respect to the static magnetic field.

2) Difference and sum: For two files (each containing data of independent measurements with shifted absorption peaks) the difference and sum between the measured signals for both files can be calculated. Additionally, a log file is created that calculates a quantification of the corresponding difference and sum (see section 4.1.1).

As one can easily see the program is rather complex, but very useful for this kind of experiments. If not mentioned differently all the displayed data was analyzed using this program.
Additionally every fit shown in this thesis was done using the C++ programming package ROOT version 5.34/18 provided by CERN [52].

4 Experimental results

In an early stage of our experiments we realized that for in-plane as well as out-of-plane magnetized YIG/graphene bilayers a voltage can be observed in the graphene layer which is clearly correlated to the excitation of spin-waves in the YIG layer. This voltage only shows non-constant values with respect to the static magnetic field for values close to the FMR-field H_0. The latter is fixed by the excitation frequency (see section 2.2.1). Magnetic fields close to this value enable an increment of absorption of electromagnetic energy and therefore an increased excitation of spin-waves.

4.1 Out-of-plane magnetized structures

The detected microwave signals for an out-of-plane magnetized structure are shown in figure 4.1. In the following we will take a closer look at the properties of the measured signals.

Absorption The absorption shown in figure 4.1a reveals that not only the uniform mode with a vanishing wave vector is excited, but a large number of wave vectors is observed. Since the YIG/graphene bilayers are magnetized out-of-plane forward volume waves are excited. The observed distribution can be explained by the dispersion relation shown in figure 2.6a. For a fixed excitation frequency the displayed spectrum is shifted to higher values for increasing magnetic fields while the general form in first approximation stays unchanged. Due to the positive dispersion, at first high wave vectors are excited. Further increment of the static magnetic field allows for lower wave vectors reaching down to the uniform mode with vanishing wave vector that is marked by the maximum absorption. The corresponding magnetic field is the FMR-field. The amplitude of the absorption for different magnetic fields can be explained by the wave vector dependent excitation efficiency of a stripline antenna that decreases for increasing wave vectors [53].
Under the reversal of the static magnetic field the measured absorption is not influenced. This matches the expectation since merely the sense of rotation around the static magnetization reverses sign, and the absorption quadratically depends on the dynamic magnetization [2, p. 201].

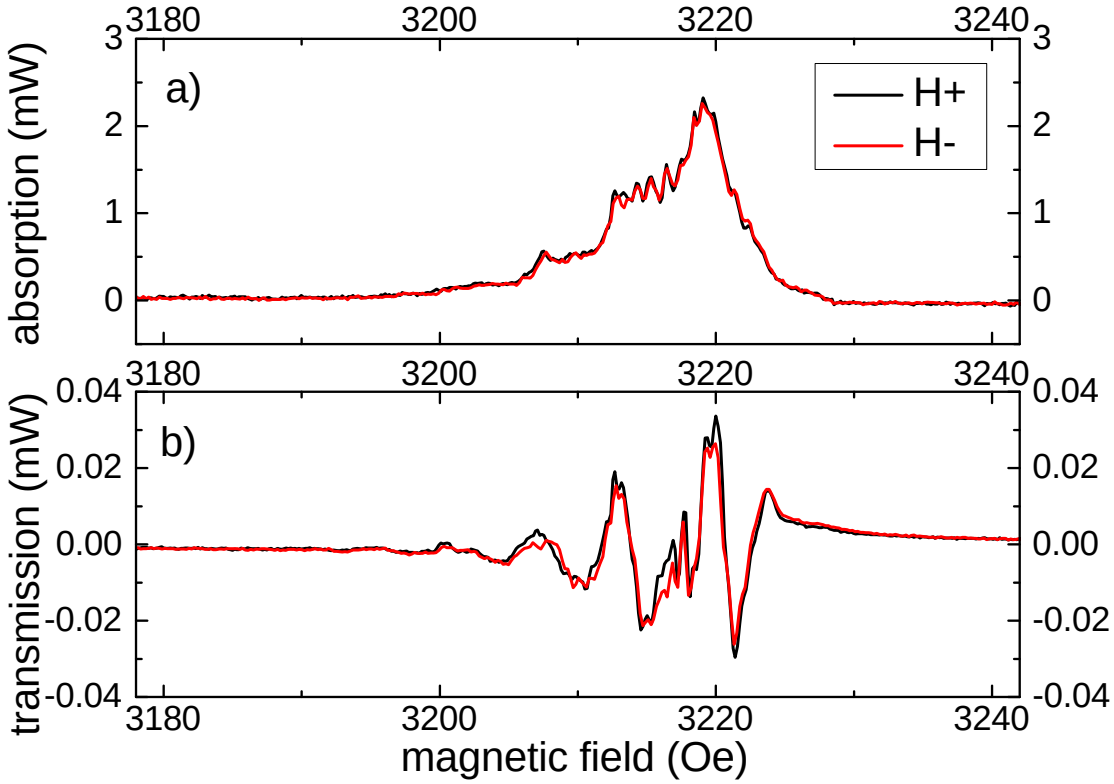

Fig. 4.1: a) Absorption and b) transmission of the microwaves for an out-of-plane magnetized structure displayed against the static magnetic field for an excitation frequency of 6.5 GHz and an excitation power of about 31.6 mW in the Cu-grown sample.

Transmission For the transmission the situation is more complex (see fig. 4.1b). Considering the absorption a broad spectrum would be expected but as can be seen the transmission is characterized by a few sharply defined peaks. This behaviour can be explained by an interference of a direct electromagnetic wave emitted by the excitation antenna and the spin-waves at the point of detection. As explained before different magnetic fields allow for different spin-wave wave vectors while the wave vector of the direct wave stays unchanged. Accordingly, the interference at the position of the second antenna depends on the applied magnetic field. A more detailed description of this behaviour will be given in section 4.2.1. This is a known phenomenon that can be verified by exciting spin-waves with a pulsed microwave-signal with a pulse length of a few nanoseconds. Using the oscilloscope the appearance of two different peaks for different transmission times is observed. The first signal corresponds to the direct wave while the second is caused by the arrival of the spin-waves. Unfortunately the reduction of the direct electromagnetic waves is very difficult. Still, to avoid unwanted absorption and stray fields every conducting ma-

terial that is not necessary for the experiments is removed. This includes thin gold cables connected to the gold contacts at the surface of the graphene layer. Only the cables necessary for the voltage detection are left. Due to the interference the true transmission signal is masked. Since the transmission antenna does not provide any helpful information this way it is removed as well to reduce disturbances.

Graphene voltage The most interesting value measured is the voltage detected in the graphene-layer between two gold contacts. In an early stage of the experiments the amplitude could only be reproduced for a few experiments. In most cases changing the gold contacts, the room temperature or other parameters could lead to strongly varying values. These fluctuations can be significantly reduced by stabilizing the sample temperature. Additionally the procedure of the measurements was changed. At first many repetitions of one experiment with the same excitation power and frequency were performed for one field direction to get a good averaged value. Then the orientation of the magnetic field was inverted and the measurements were repeated to compare the results for both field directions. This method proved to be very sensitive to hysteresis phenomena and long term effects. A great improvement could be reached by immediately changing the orientation of the static magnetic field after every measurement as described in section 3.2. Due to the improved data quality the number of repetitions could be significantly reduced. In most cases even a single measurement would be sufficient, but this way the reproducibility can be ensured.
The examination of the appearing voltage will be the main part of this thesis. Although the general behaviour is the same for every gold contact and both samples every following graphic will use results gained from examination of the Pt-grown sample for a better comparability. We begin with the voltage measured along the direction of spin-wave propagation in the following referred to as longitudinal voltage.

4.1.1 Longitudinal voltage

To analyze the longitudinal voltage the contacts A and B or C and D in figure 4.2 can be used. We begin with out-of-plane magnetized films. For an adequate description of the observed phenomena we define a coordinate system. The direction of spin-wave propagation defines the x-axis, the in-plane component perpendicular to the first direction defines the y-axis and the out-of-plane component is the z-axis (see fig. 4.2).
As mentioned before, for out-of-plane magnetized structures a voltage measured along the direction of spin-wave propagation can be observed that is clearly correlated to the excitation of spin-waves. An example for an excitation frequency of 5.8 GHz and an excitation power of about 31.6 mW is shown in figure 4.3. Both, the absorption of microwave energy and the voltage only show non-constant values for

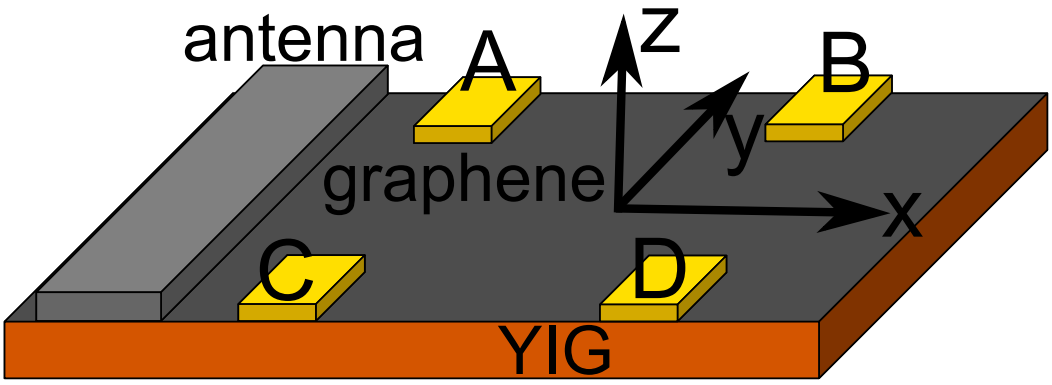

Fig. 4.2: Coordinate system.

static magnetic fields that allow for excitation of spin-waves. Additionally the voltage reveals a fascinating behaviour under inversion of the orientation of the static magnetic field:
The graphene-voltage for the first direction - in the following referred to as the positive orientation H+ - does not show the same trend as for the second (negative) orientation H-. Since it is neither completely symmetrical or antisymmetrical with respect to the orientation of the static magnetic field it is plausible to assume that a combination of a symmetrical V_{sym} and an antisymmetrical graphene-voltage V_{antisym} originating in different effects is observed. To be able to analyze both voltage components independently they have to be separated by calculating the difference and the sum of the measured curves divided by two:

$$V_{\text{sym}}(H) = [V(H) + V(-H)]/2 \tag{4.1}$$
$$V_{\text{antisym}}(H) = [V(H) - V(-H)]/2 \tag{4.2}$$

The results with respect to the static magnetic field are shown in figure 4.4. Both components reveal a clear dependence on the absorption. This becomes particularly visible in the double peak structure with the corresponding maxima at about 3820 Oe and 3810 Oe that can be observed in the absorption and both voltage components. The peak at 3820 Oe is the uniform mode that corresponds to the standard FMR-field as described in section 2.2.1. The additional peak at 3810 Oe is probably caused by a transversal mode that appears due to the limited YIG-layer width that acts as a resonator for transversal wave vectors. For a magnetic field of about 3800 Oe the existence of an additional peak can be observed but with much lower amplitude. Especially for the symmetric voltage this peak is still visible.
In the following we will try to understand the origin of the observed symmetric as well as the antisymmetric voltage.

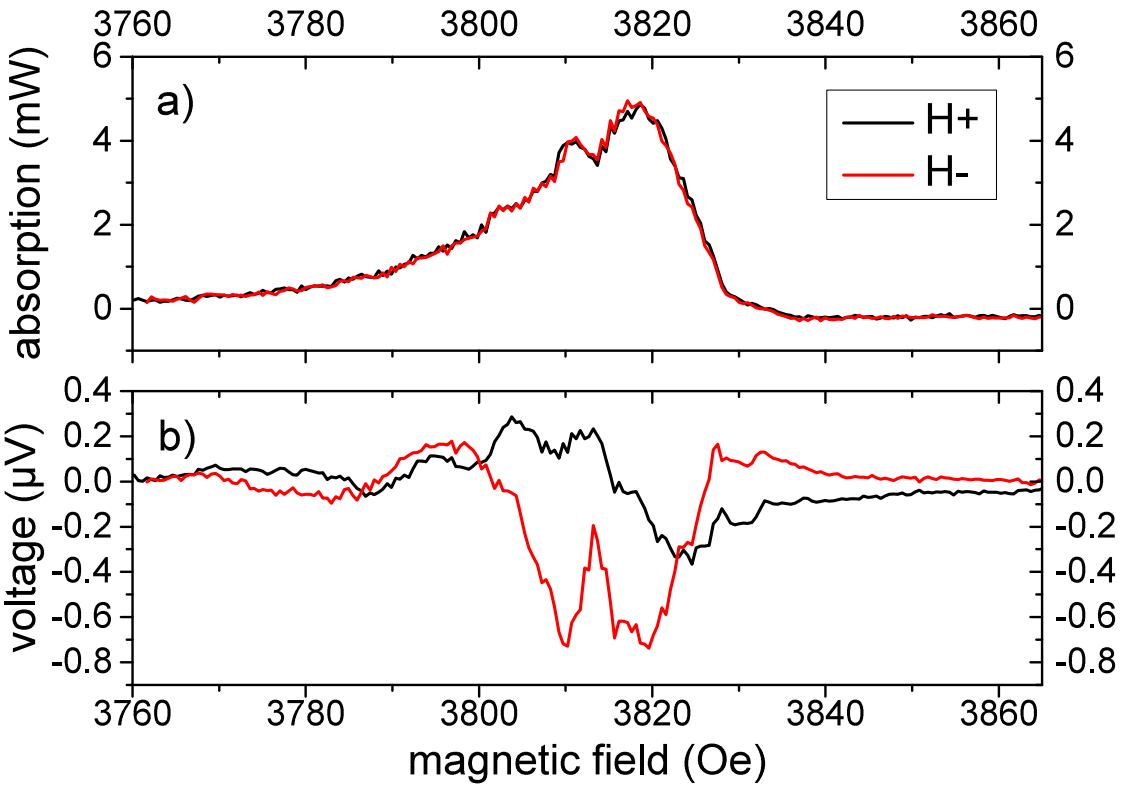

Fig. 4.3: a) Absorption and b) longitudinal voltage for out-of-plane magnetized structures with an excitation frequency of 5.8 GHz and an excitation power of about 31.6 mW.

Symmetric voltage

The symmetric voltage can be explained by several known effects. The offset is most certainly caused by induced currents in the graphene layer originating in the direct electromagnetic wave emitted by the antenna. A Schottky barrier between the semiconducting graphene and the gold contacts leads to a rectification [54] so that a non-vanishing dc-value can be observed. The intensity difference at the position of the contacts due to the decreasing amplitude of the direct wave with increasing distance from the antenna creates a voltage difference between the contacts that can be detected by our setup. The offset in this case has a value of -5.5 μV and is accordingly much larger than the observed values in figure 4.4c).
For magnetic fields that allow for spin-wave excitation additional currents in the graphene layer could be induced but this is rather unlikely. For out-of-plane magnetized structures the dynamic magnetization of the spin-waves is in-plane and so are the dynamic magnetic fields. According to Faraday's induction law this configuration does not lead to induction of currents in the graphene layer [21, p.212].

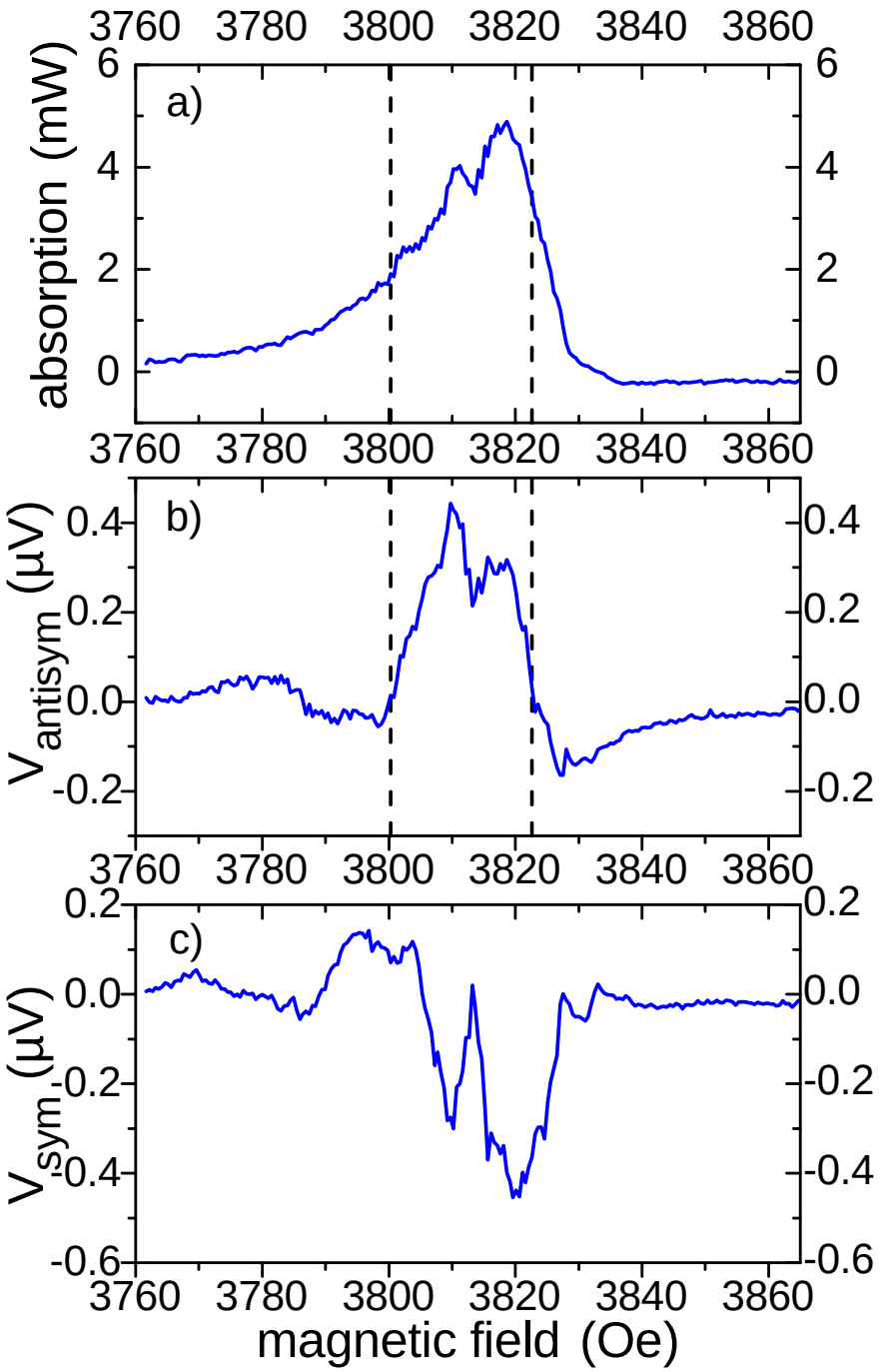

Fig. 4.4: a) Mean absorption of both field directions, b) antisymmetric voltage and c) symmetric voltage displayed against the static magnetic field for an excitation frequency of 5.8 GHz and an excitation power of about 31.6 mW. The dashed lines mark the integration limits used to determine the power dependence of the antisymmetric voltage.

In section 4.2.1 we will come back to this in more detail.
The main part of the symmetric voltage in figure 4.4c) is probably connected to a temperature gradient along the direction of spin-wave propagation created by the damping of spin-waves. Close to the antenna the spin-wave amplitude has its largest value and accordingly the energy flow from the magnetic subsystem to the lattice is most pronounced here. This creates a heat current that due to the *Seebeck effect* is expected to lead to a voltage along the direction of the gradient [10, p. 259] [55]. The Seebeck effect can be briefly explained as follows: In the presence of a temperature gradient electrons and holes on the hot end of the material move to the cold end. The different charge carrier mobilities and concentrations lead to an electric field

$$\vec{E} = S \cdot \nabla T \tag{4.3}$$

with S as the so called *thermoelectric power* or *Seebeck coefficient* [56, p.346]. In our case the voltage is measured at the gold contacts. Since these graphene/Au heterojunctions have different temperatures they form a thermocouple as shown in figure 4.5. The corresponding Seebeck voltage can be calculated to be

$$V_{\text{Seebeck}} = \int_{T_1}^{T_2} (S_{\text{graphene}} - S_{\text{Au}}) dT \tag{4.4}$$

with T_i as the temperature of the i-th contact [10, p. 259] and accordingly $T_1 > T_2$. Since the thermoelectric powers S_{graphene} and S_{Au} can be estimated to be constant in the low temperature range (see below) used in these experiments we have

$$V_{\text{Seebeck}} \approx -(S_{\text{graphene}} - S_{\text{Au}}) \cdot \Delta T. \tag{4.5}$$

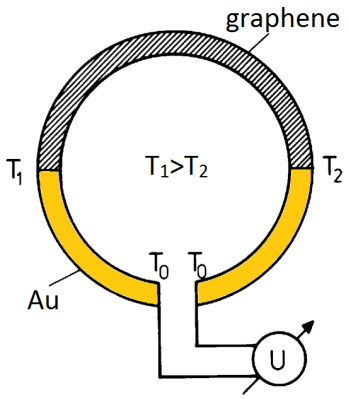

Fig. 4.5: Thermocouple consisting of two gold contacts and the graphene layer. Modified from [10, p. 259].

The existence of the temperature gradient was observed using an infrared camera (see fig. 4.6). To verify that the detected gradient is not caused by Ohmic heating of the antenna the static magnetic field is slightly changed so that no spin-wave excitation is possible. In this case the temperature difference vanishes so that the damping of spin-waves has to be the origin of the gradient.
While for gold the thermoelectric power at room temperature is simply given by $1.94\,\mu V/K$ [57, p. 167] the determination of the value of graphene is more difficult. The thermoelectric power in graphene strongly depends on the energy difference of the Fermi level in the graphene layer relative to the Dirac points. For vanishing difference the Seebeck coefficient is expected to be zero since the mobility and concentration of holes and electrons in this case is equal [55]. The graphene layers used in our experiments are determined to be slightly p-doped due to lattice defects. Accordingly, the Fermi-level is below the Dirac point, and S_{graphene} is expected to be positive. From [55] the value can be estimated to be a few $10\,\mu V/K$. This matches the observations since the symmetric voltage is negative, and therefore we have $S_{\text{graphene}} > S_{\text{Au}}$. Since we observe voltages of maximum values of a few μV on a contact distance of about 1.3 mm for high excitation powers and a corresponding temperature gradient of about $0.1\,K/mm$ the order of magnitude can be reproduced by this theory.
Further information on the symmetric voltage can be gained from close observation of the double peak structure. One can see that the voltage reduces to approximately zero between the peaks. Since the variation in the absorption is rather small this is not expected to have such a strong influence. The explanation is a reduced offset for magnetic fields that allow for spin-wave excitation. In this case not the total energy emitted by the antenna is radiated in form of a direct wave so that the amplitude of the induced currents in the graphene layer is reduced and so is the offset. Accordingly, the actual Seebeck voltage is expected to be significantly larger than the observed voltage. Since the offset reduction cannot be quantified the actual value of the Seebeck voltage is difficult to determine.

Antisymmetric voltage

For the antisymmetric voltage the situation gets more complicated. For out-of-plane magnetized YIG/graphene bilayers it seems that no theory exists so far that predicts the appearance of a voltage along the direction of spin-wave propagation that reverses sign under inversion of the static magnetic field. Accordingly, more information is needed to understand the measurements.
As mentioned before the double peak structure detected for the absorption can also be found in the antisymmetric voltage revealing a clear dependence on the excitation of spin-waves. For magnetic fields above the FMR-field we observe a contribution to the antisymmetric voltage with a negative sign that can reach magnitudes that are comparable but always smaller than the actual antisymmetric voltage. Since

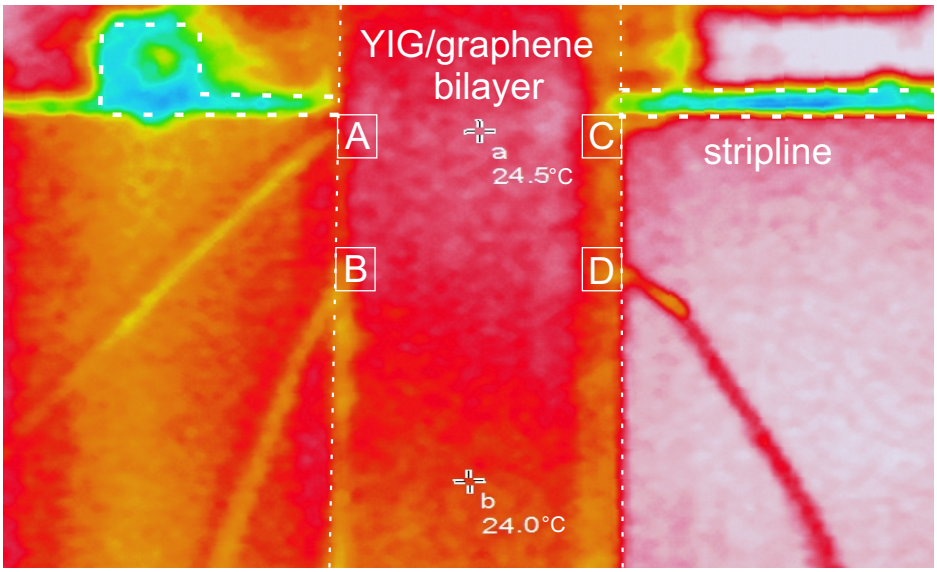

Fig. 4.6: Temperature gradient caused by the damping of spin-waves for an excitation frequency of 3 GHz and an excitation power of 100 mW.

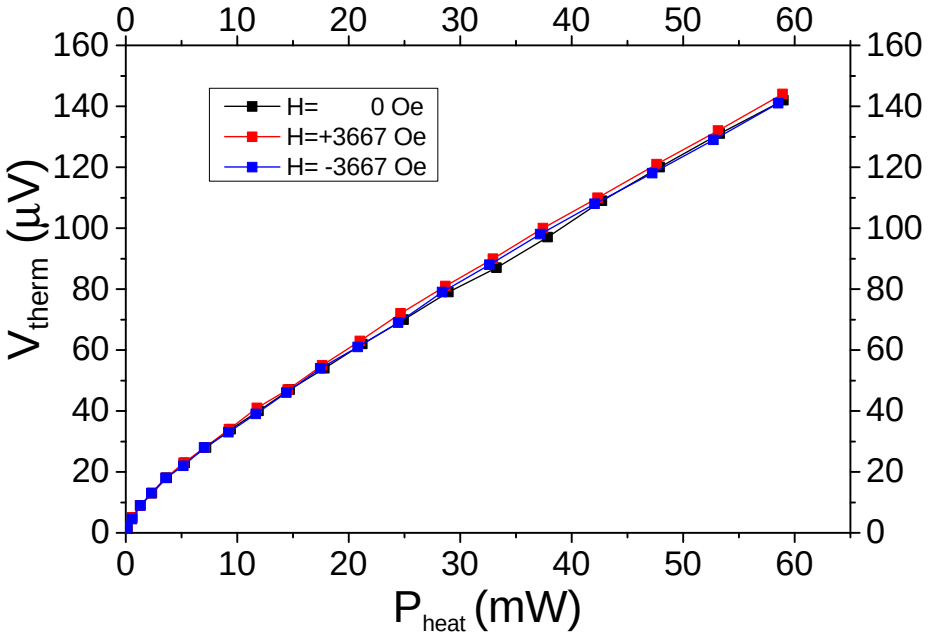

Fig. 4.7: Voltage along the direction of the temperature gradient caused by Ohmic heating due to a dc-current displayed against the heating power for an out-of-plane bias field of (black) 0 Oe, (red) 3667 Oe and (blue) -3667 Oe.

predictions and explanations of the spin-wave properties for these magnetic fields are rather difficult these regions are excluded from the analysis. Sign changes for lower magnetic fields are typically less pronounced and could be an uncertainty.
Since the currents induced by the direct wave are independent of the orientation of the static magnetic field the voltage offset is expected to equal for both field directions. Accordingly, the offset has to be zero which matches the measured value.
In the following we will present two conceivable explanations of the observed effect.

a) Spin-wave mediated thermoelectric effect A first assumption was a spin-wave mediated thermoelectric effect that had not been described so far. The temperature gradient would be as mentioned before caused by the damping of spin-waves and accordingly only appear for static magnetic fields close to the FMR-field. To match the observation the voltage measured along the direction of the heat current would then have to depend on the orientation of the static magnetic field. To verify this idea a temperature gradient was created by Ohmic heating in a cable on the YIG/graphene bilayer. The cable was heated using a dc current so no spin-waves could be excited. Additionally a static magnetic field was applied. Measurements show that the reversal or even the removal of the magnetic field does not lead to an antisymmetric voltage as can be seen in figure 4.7. Accordingly, a spin-wave mediated thermoelectric effect can be excluded as the origin of the antisymmetric voltage.

b) Spin-wave mediated magnetoelectric effect Another idea was a spin-wave mediated magnetoelectric effect. To describe the effect equation (2.37) can be modified:

$$E_i = \alpha_{ij}^{\mathrm{E}}[H(\omega_0)] \cdot H_j. \tag{4.6}$$

The electric field E_i in the graphene layer leads to the observed voltage in the gold contacts. The linear relation of the magnetic field vector and the electric field vector fulfils the condition that the inversion of the static magnetic field causes the voltage sign to reverse as well. The tensor only shows non-vanishing values for magnetic fields that allow for spin-wave excitation. The corresponding interval is determined by the excitation frequency ω_0.
To get a better understanding of this effect further experiments are needed. Different measurement geometries give access to different components of the tensor. Rows can be analyzed by varying the contacts on the graphene layer so that a voltage can be measured along the x- or y-axis. The columns are selected by the orientation of the static magnetic field. For out-of-plane magnetized structures with the voltage measured along the x-axis only the tensor component α_{13}^{E} contributes to the measured voltage.
Since we assume the effect to be connected to the excitation of spin-waves we will

examine the frequency and power dependence of the measured voltage.

Power dependence

To study the dependence of the discovered effect on the excitation power of spin-waves the frequency is fixed and the static magnetic field is scanned in fixed intervals for different excitation powers.
The easiest method to quantify the efficiency of the effect would be to read out the maximum value of the antisymmetric voltage and compare it to the absorption of microwaves at the same magnetic field. Since the analysis of a single point can be very sensitive to fluctuations this might not be the best idea. Therefore, we decided to integrate the voltage in the interval between the first voltage sign changes around the maximum of absorption and compare it to the integral of the absorption in the same interval. An example of these integration limits is shown in figure 4.4. The sign changes are chosen as integration limits as these points indicate other contributions with opposite sign that start dominating the voltage. The low limit typically corresponds to magnetic fields with fewer microwave absorption and spin-wave excitation. Accordingly, the contribution to the voltage in this region is rather small. Since we are looking for a spin-wave mediated effect we focus on regions that are mainly determined by strong spin-wave excitation and exclude other parts from our analysis. The upper limit can be found above the FMR-field. As already mentioned the spin-wave properties are rather complicated in this scope so that these regions are excluded from the analysis by the chosen integration limits as well.
If we display the integrated voltage against the integrated absorption we see that the relation between these value shows a clear linear relation as can be seen in figure 4.8 for three different frequencies. The lines displayed are linear fits with vanishing offset demonstrating good agreement with the measured data. The situation looks very similar for different frequencies. This tendency has proved to be stable against changes of the analysis method. Even if only the point of maximum voltage is analyzed or if the integration limits are set to a low percentage value of the absorption the general behaviour stays the same.
A spin-wave property that has a linear dependence on the absorbed energy is the current of magnons from the antenna along the direction of spin-wave propagation. A magnon is the quasi particle that can be used to describe spin-waves [2, pp. 199]. A single magnon represents an excitation of the ferromagnetic ground state. In the ground state every electron spin is aligned parallel. The first excitation is the reversal of a single spin. Due to the exchange interaction this is a energetically highly unfavourable state so that the total reversed spin is averaged over the ferromagnet. Accordingly, every spin is only slightly detuned from the equilibrium orientation [10, pp.214]. This is the quantum mechanical description of a spin-wave. The propagation direction of magnons is defined by the direction of the group velocity. Like the absorption the number of magnons excited in the system depends on the squared

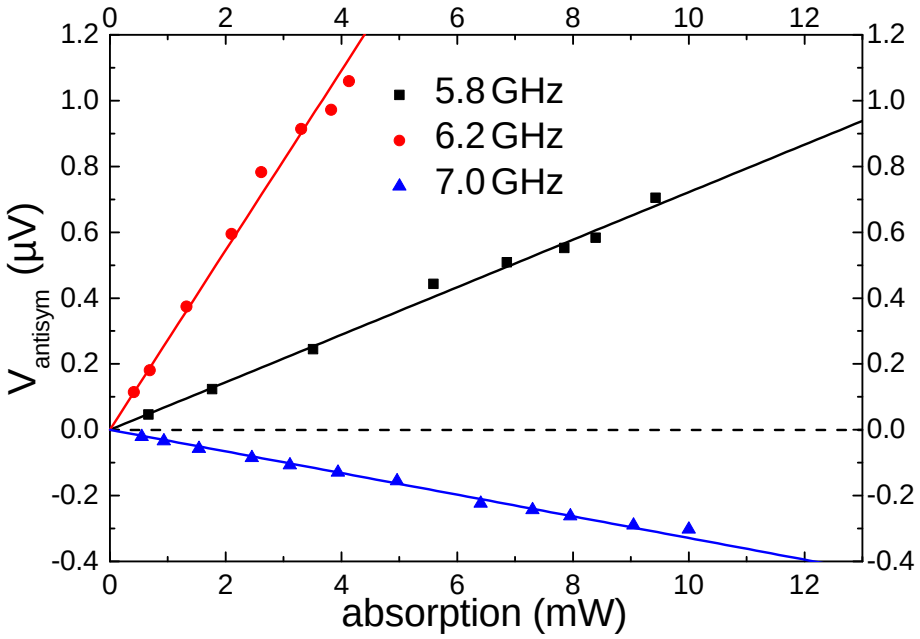

Fig. 4.8: Integrated antisymmetric voltage displayed against the integrated absorbtion in the same interval. The lines are linear fits with vanishing offset.

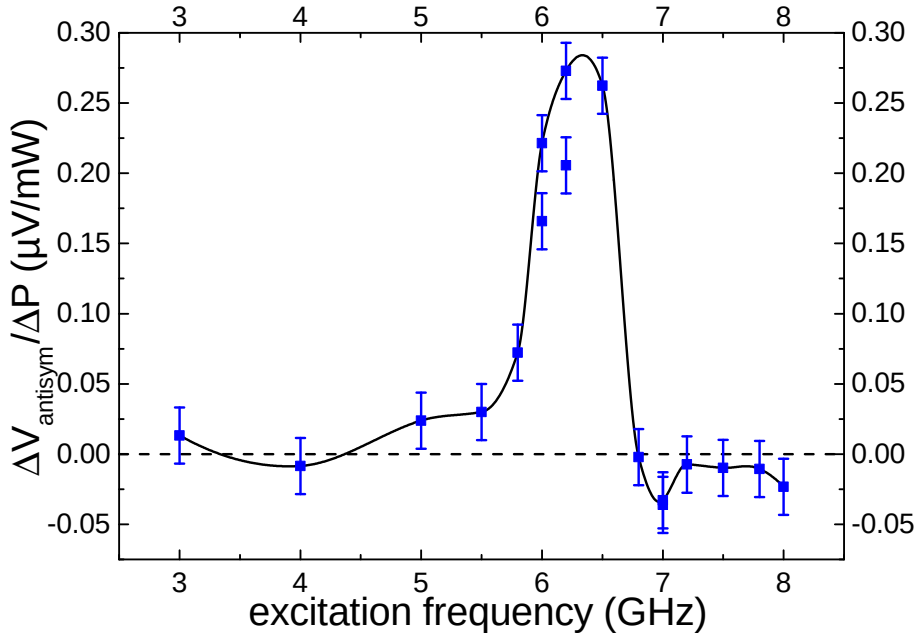

Fig. 4.9: Slope of the linear fits to the integrated antisymmetric voltage vs the integrated absorption displayed against the excitation frequency. The black line is merely to guide the eye.

dynamic magnetization $\vec{m}$ [2, p.201] so that the current of magnons linearly depends on the absorption.

Frequency dependence

Another fascinating finding is that the magnitude of the increment of the antisymmetric voltage with respect to the absorption depends on the excitation frequency. Furthermore, the sign changes from positive to negative for frequencies above 6.8 GHz. This sign change was verified in different measurements and is not connected to an uncertainty caused by the low voltages in this region. To gain a better understanding of this behaviour we display the slope determined from the linear fits of the detected voltage with respect to the absorption against the excitation frequency (see fig. 4.9). The graphic reveals a clear resonant behaviour around the maximum at about 6.2 GHz. The negative part for higher frequencies indicates an admixture of the derivative of the standard Lorentz curve. This is a known phenomenon for resonance experiments. A surprising property of this curve is the resonance frequency of several GHz. Typically magnetoelectric resonances are found in the kHz domain [1] since for example mechanical eigenmodes enable a maximum coupling between the electric and magnetic field for layered structures. While tuneable microwave properties using an electric field are a known phenomenon (see for example [29]) magnetoelectric resonances for microwaves as excitation frequency have not been observed so far to the best of our knowledge. This suggests that no mechanical eigenmodes are responsible for this effect. Additionally we see that the tensor in equation (4.6) not only depends on the excitation frequency to match the resonance magnetic field. The choice of the excitation frequency strongly influences the amplitude of the tensor.

4.1.2 Transversal voltage

Using out-of-plane magnetized films measuring the longitudinal voltage the only contributing tensor component is α^{E}_{13}. To determine the basic process responsible for the observed antisymmetric voltage the examination of further components and accordingly further measurement geometries are needed. Therefore, we will continue with the voltage transversal to the direction of spin-wave propagation. For out-of-plane magnetized structures ($j = 3$) with the voltage measured along the y-axis ($i = 2$) the only contributing component is α^{E}_{23}. The experimental results are shown in figure 4.10. As expected the absorption looks very similar to the measurements for the longitudinal voltage and is independent of the orientation of the static magnetic field.

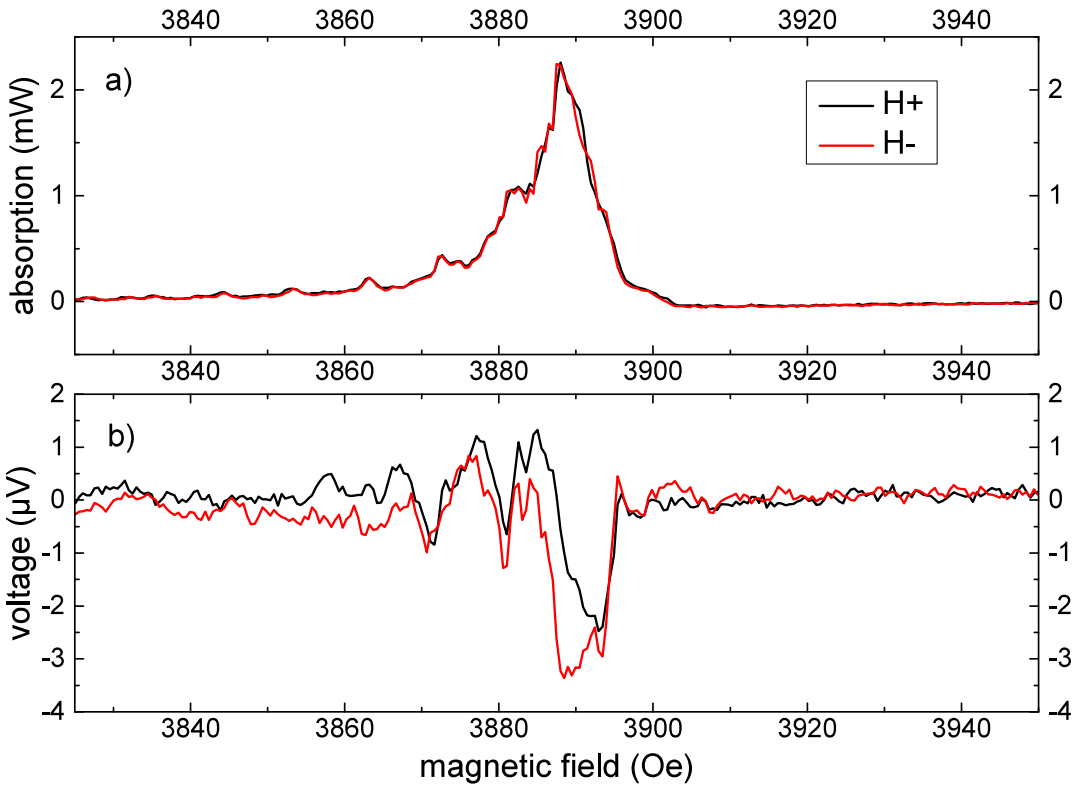

Fig. 4.10: a) Absorption and b) voltage for out-of-plane magnetized structures with the voltage measured perpendicular to the direction of spin-wave propagation. The exctiation frequency is 6 GHz and the excitation power about 31.6 mW.

Symmetric voltage

Since the voltage is measured perpendicular to the direction of spin-wave propagation and to the direction of the temperature gradient the Seebeck effect can be excluded as the origin of the detected voltage. A probable explanation is again the induction of currents caused by the direct electromagnetic wave. Since the used contacts A and C (see fig. 3.1) are very close to the antenna the induction is very high which can be seen in the offset of about 22.6 µV. Again for magnetic fields that allow for excitation of spin-waves it is expected that the amplitude of the direct wave is reduced. This matches the observations since the absorption reveals peaks with increased absorption that correspond to the excitation of several transversal spin-wave modes. For the corresponding magnetic fields a more negative voltage is observed indicating a reduced induction which matches the expectations.

Antisymmetric voltage

In contrast to the longitudinal voltage the transversal voltage does not show an antisymmetric component. Although the amplitudes do not match perfectly, the trend of both curves is always the same for every applied magnetic field. The small variations are most certainly nothing more than an uncertainty. This behaviour can be observed for different frequencies. A large contribution of the Nernst effect is rather unlikely. The Nernst effect is a combination of the Seebeck effect and the Hall effect leading to an antisymmetric voltage under the inversion of the magnetic field that is oriented out-of-plane. The corresponding electric field is oriented perpendicular to the direction of the temperature gradient. Although the geometry of this measurement matches the requirements of the Nernst effect, in graphene this effect is only strongly pronounced for magnetic fields of several Tesla which is by an order of magnitude larger than the fields used in our experiments [58].
As a consequence the tensor component α_{23}^{E} vanishes. This means that the spin-wave mediated magnetoelectric effect for out-of-plane magnetized structures does not lead to a voltage perpendicular to the direction of spin-wave propagation. The vanishing transversal antisymmetric voltage also provides the information that the voltage in the contacts A and C as well as B and D is equal. This means that the longitudinal antisymmetric voltage is independent of the side on which the voltage is measured.
In the following section we will examine the consequences of the vanishing transversal voltage on the symmetry properties of the analyzed effect.

4.1.3 Symmetry considerations

If we consider the symmetry properties of the magnetoelectric effect the tensor has to break time reversal and spatial inversion symmetry simultaneously as we have seen in equation (2.36). From the linear power dependence of the detected voltage we already saw that the current of magnons $\vec{\phi}^{\mathrm{m}}$ is a possible candidate for this behaviour. Its symmetry properties also match the expectations:

1. Since $\vec{\phi}^{\mathrm{m}}$ is a true vector it fulfils the requirement to reverse sign under spatial inversion.
2. The time reversal symmetry is broken since $\vec{\phi}^{\mathrm{m}}$ is a current and therefore flows backwards under temporal inversion.

Due to the vanishing transversal voltage it seems that the current of magnons also defines the direction of the electric field and accordingly the measured voltage.

y-inversion symmetry

Since the voltage is equal on both sides of the structure an additional symmetry has to be considered. If we mirror the sample at the xz-plane we project the sample onto

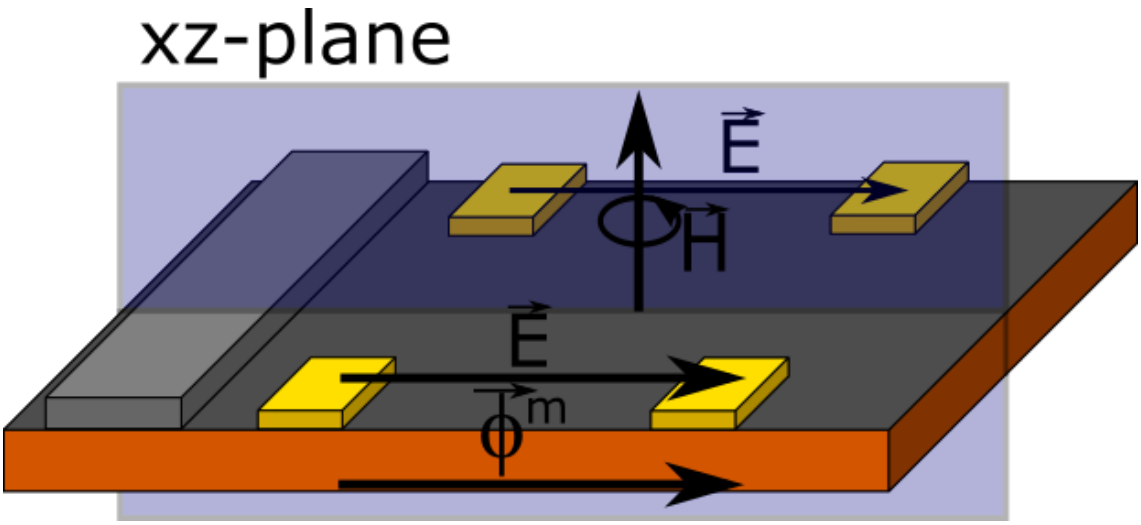

Fig. 4.11: Inversion of the y-axis or mirroring the sample at the xz-plane (blue plane) leaves the electric field $\vec{E}$ or the current of magnons $\vec{\phi}^{\mathrm{m}}$ unchanged but reverses the static magnetic field $\vec{H}$ since it is an axial vector.

itself (see fig. 4.11). Therefore, the voltage, the electric field as well as the current of magnons stay unchanged. For the magnetic field the situation is different. The magnetic field is an axial vector and therefore reverses its sign under the inversion of a single axis perpendicular to the vector:

$$\hat{I}_{\mathrm{y}} E_i = \hat{I}_{\mathrm{y}} \left(\alpha^{\mathrm{E}}_{ij} H_j\right) \tag{4.7}$$

$$\Rightarrow E_i = \alpha^{\mathrm{E}}_{ij} \cdot \hat{I}_{\mathrm{y}} H_j \tag{4.8}$$

$$\Rightarrow E_i = -\alpha^{\mathrm{E}}_{ij} H_j \tag{4.9}$$

with $\hat{I}_{\mathrm{y}}$ as the operator for the inversion of the y-axis. We see that the electric field changes sign if we assume the tensor to be invariant under inversion of the y-axis. Since this is a violation to the observation the effect has to break the y-inversion symmetry and the tensor has to change sign. As already mentioned this cannot be caused by the magnon current. This leads to the conclusion that a second property is needed that reverses sign under inversion of the y-axis, but not under the inversion of all spatial axes since this is already provided by the flow of magnons. A material property that fulfils this requirement is the screw dislocation with the displacement vector along the z-axis. A screw dislocation is a crystallographic defect with special properties. For every revolution around the vector in the direction of displacement a new layer of atoms is reached [9, p. 657]. As already mentioned in section 2.3.2 a screw structure is invariant under spatial inversion, but reverses sign if only one component perpendicular to the rotational axis is revered. Due to its symmetry properties the screw structure is - like the magnetic field - an axial vector.

A possible origin of the observed phenomena could be that the presence of the screw dislocation at the surface leads to a deformation of the graphene layer. Since the electronic properties of graphene are very sensitive to deformation it is possible that this deformation creates an antisymmetric electronic state. Under the influence of spin-waves this state leads to a measurable voltage along the direction of spin-waves that reverses sign under inversion of the static magnetic field. Still, up to now this is merely speculation.

4.1.4 YIG/aluminium bilayers

To determine if the observed effect can also appears for other materials we will examine YIG/aluminium bilayers in this section. To compare YIG/aluminium bilayers with previous measurements the structures are magnetized out-of-plane and contacted along the direction of spin-wave propagation. Measurements reveal that the absorption is very similar for YIG/graphene and YIG/aluminium bilayers as expected (see fig. 4.12).

Symmetric voltage

The symmetric voltage is again accompanied by an offset that in the displayed case has a value of about -3.8 µV. Like for YIG/graphene bilayers the offset is probably caused by the direct electromagnetic wave that induces a current in the aluminium layer. To be able to detect a dc voltage we need a rectification process. This can be caused by a layer of aluminium oxide (Al_2O_3) that typically covers aluminium layers forming a tunnelling barrier between the aluminium layer and the gold contacts [59]. Like for YIG/graphene bilayers the origin of the symmetric voltage is again the Seebeck effect as described in section 4.1.1. Taking a look at the amplitude of the voltage we see that it is by one order of magnitude smaller than the observed values in the graphene layer. With a Seebeck coefficient of aluminium at room temperature of -1.66 µV/K [57, p. 167] it can be estimated that the observed voltage is of the expected order of magnitude.
Additionally, the excitation of spin-waves reduces the induced voltage. Since the offset is negative this leads to more positive voltages with respect to the offset and the amplitude of the detected voltage is reduced.

Antisymmetric voltage

The antisymmetric voltage cannot be observed in YIG/aluminium bilayers. All the measured values are equal within the statistical uncertainty. This behaviour can be observed for both samples and different frequencies. There are two possible explanations why a YIG/graphene bilayer is sensitive to the observed effect and the

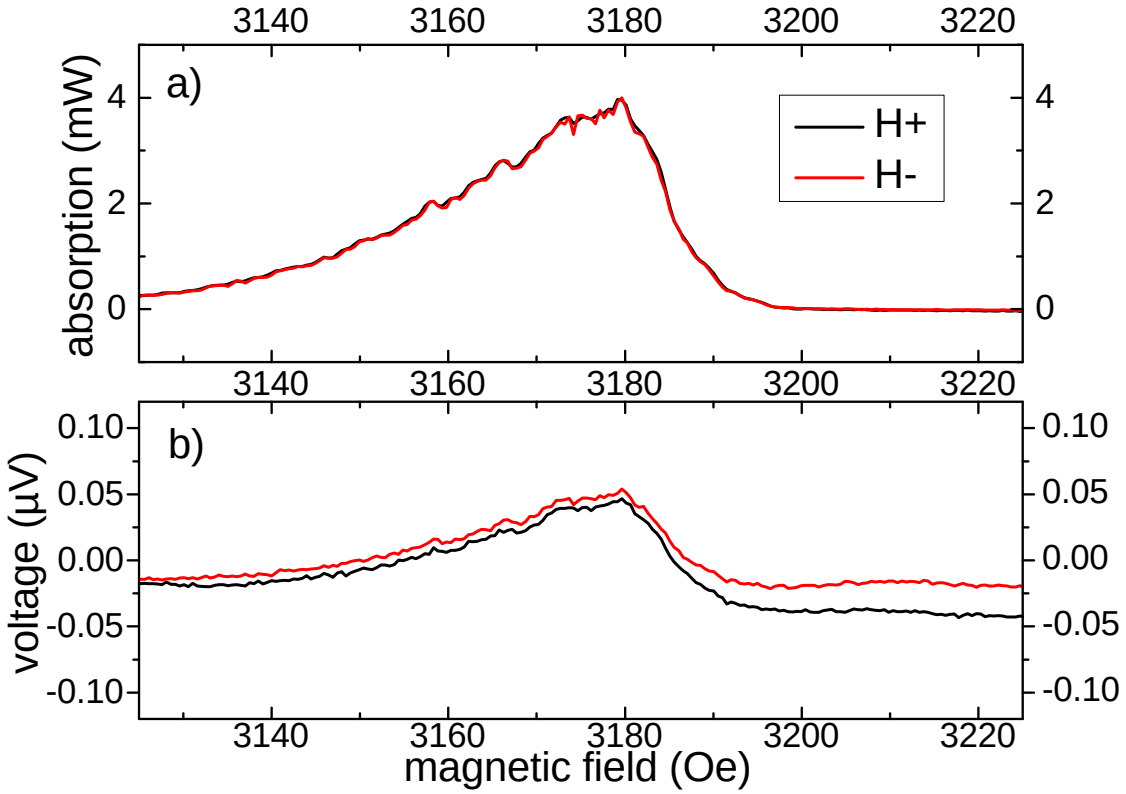

Fig. 4.12: a) Absorption and b) voltage along the direction of spin-wave propagation for out-of-plane magnetized YIG/aluminium bilayers for an excitation frequency of 4GHz and an excitation power of about 31.6 mW.

used YIG/aluminium bilayers are not. The first possibility is material properties of graphene that lead to the observed phenomenon that are not present in aluminium. The second idea is that the observed effect is mediated by the interface of the layers and is therefore a surface effect. Accordingly, the detected voltage should be more pronounced for thinner layers especially since the voltage is measured on top of the aluminium or graphene layer. As we have seen in section 2.3.3 the volume ratio of the contributing layers can strongly influence the magnetoelectric response. Still, it cannot be excluded that both theories contribute to the observed behaviour.

4.2 In-plane magnetized bilayers

Since we assume a screw dislocation in the YIG layer oriented along the z-axis to be the origin of the antisymmetric voltage it might be interesting to investigate the behaviour of the effect if the magnetization is not parallel to the z-axis. Therefore, we will continue with in-plane magnetized YIG/graphene bilayers. For out-of-plane magnetized YIG/graphene bilayers the situation is simple since the magnetic field is always perpendicular to the direction of spin-wave propagation and the measured voltage. For in-plane magnetized structures the situation is more complex. An orientation of the static magnetic field perpendicular to the direction of spin-wave propagation leads to the excitation of Damon-Eshbach modes. The problem with this geometry is that these spin-wave modes are non-reciprocal under the inversion of the static magnetic field, meaning that only the propagation in one direction from the point of excitation is efficient [60]. Accordingly, the detected voltage vanishes for one orientation of the static magnetic field and different field orientations cannot be compared. Therefore, tensor components of α_{ij}^{E} with $j = 2$ cannot be determined. In this thesis we will focus on a simpler case. The static magnetic field is applied along the x-axis and is therefore aligned parallel to the direction of spin-wave propagation. This way backward volume waves are excited in the YIG layer and tensor components with $j = 1$ can be examined. Like for out-of-plane magnetized structures we begin with the analysis of the longitudinal voltage. The absorption and the voltage are displayed in figure 4.13 for both field directions.

Absorption

If we take a look at the absorption we see that for both field directions the measurements do not show any differences as expected. Another property revealed by the measured absorption is that the spectrum looks very similar to the forward volume spectrum, but mirrored at the point of maximum spin-wave excitation. The reason for this is the negative dispersion of backward volume waves. In this case higher fields are needed to excite higher wave vectors while for FVMSWs the situation is the other way around. Also the magnetic field needed to excite the uniform mode for $k = 0$ is much lower since no demagnetizing field has to be compensated for in-plane magnetized structures (see equation (2.20) and (2.21)).

4.2.1 Longitudinal voltage

Although the absorption of in-plane magnetized bilayers shows a comparable behaviour to the absorption observed for out-of-plane magnetized structures the graphene voltage is very different. The data shown in figure 4.13 reveal that an antisymmetric voltage is present in these measurements, but the detected voltage is

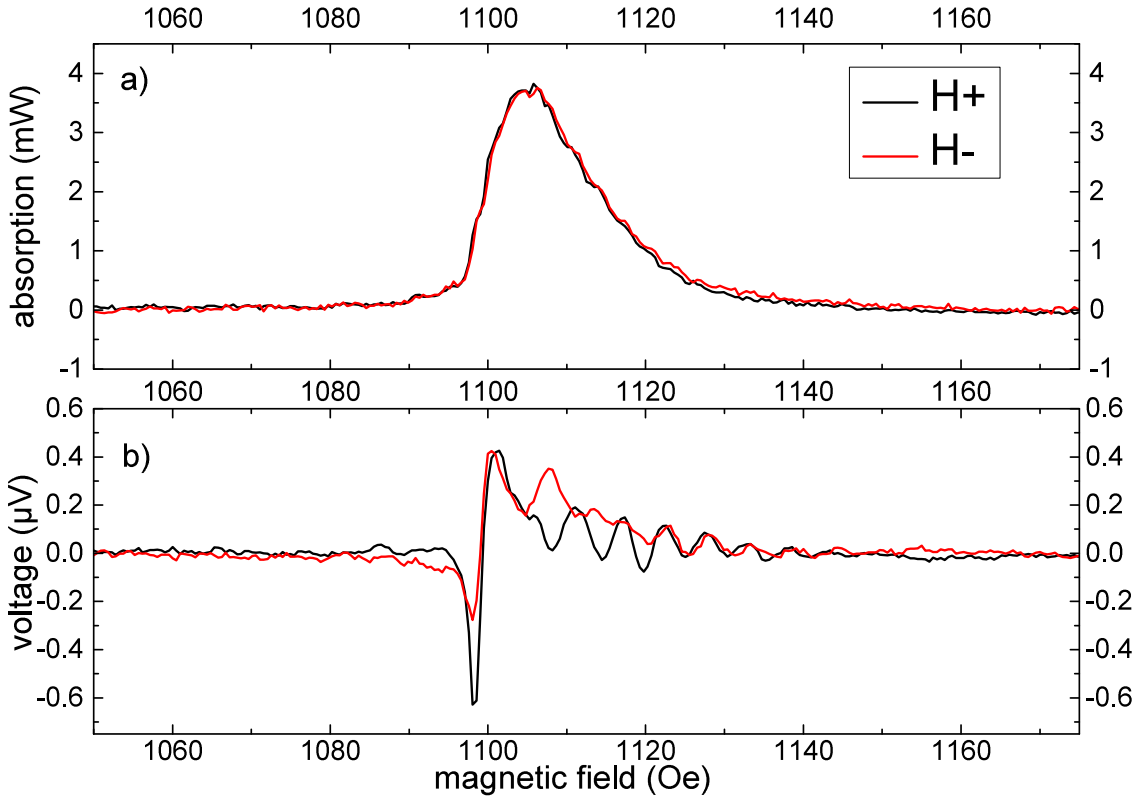

Fig. 4.13: a) Absorption and b) longitudinal voltage for in-plane magnetized structures with an excitation frequency of 5 GHz and an excitation power of about 31.6 mW.

dominated by oscillations that could not be observed for out-of-plane magnetized structures. In the following we will try to understand if these oscillations are caused by the spin-wave mediated magnetoelectric effect that was proposed for out-of-plane magnetized structures or if we observe a different phenomenon.

Symmetric voltage

The symmetric voltage shown in figure 4.14c) for magnetic fields above the FMR-field can again be explained by the Seebeck effect. Additionally the reduced induction caused by the direct wave has to be considered. For higher magnetic fields again oscillations can be observed that are most certainly caused by the appearance of transversal spin-wave modes as it could already be observed for the transversal voltage measured for out-of-plane magnetized structures (see section 4.1.2). Here the amplitude of the direct wave is reduced due to an increased excitation of spin-waves. The presence of these modes is indicated in the absorption in small variation. For magnetic fields close to the FMR-field these oscillations are partly masked by

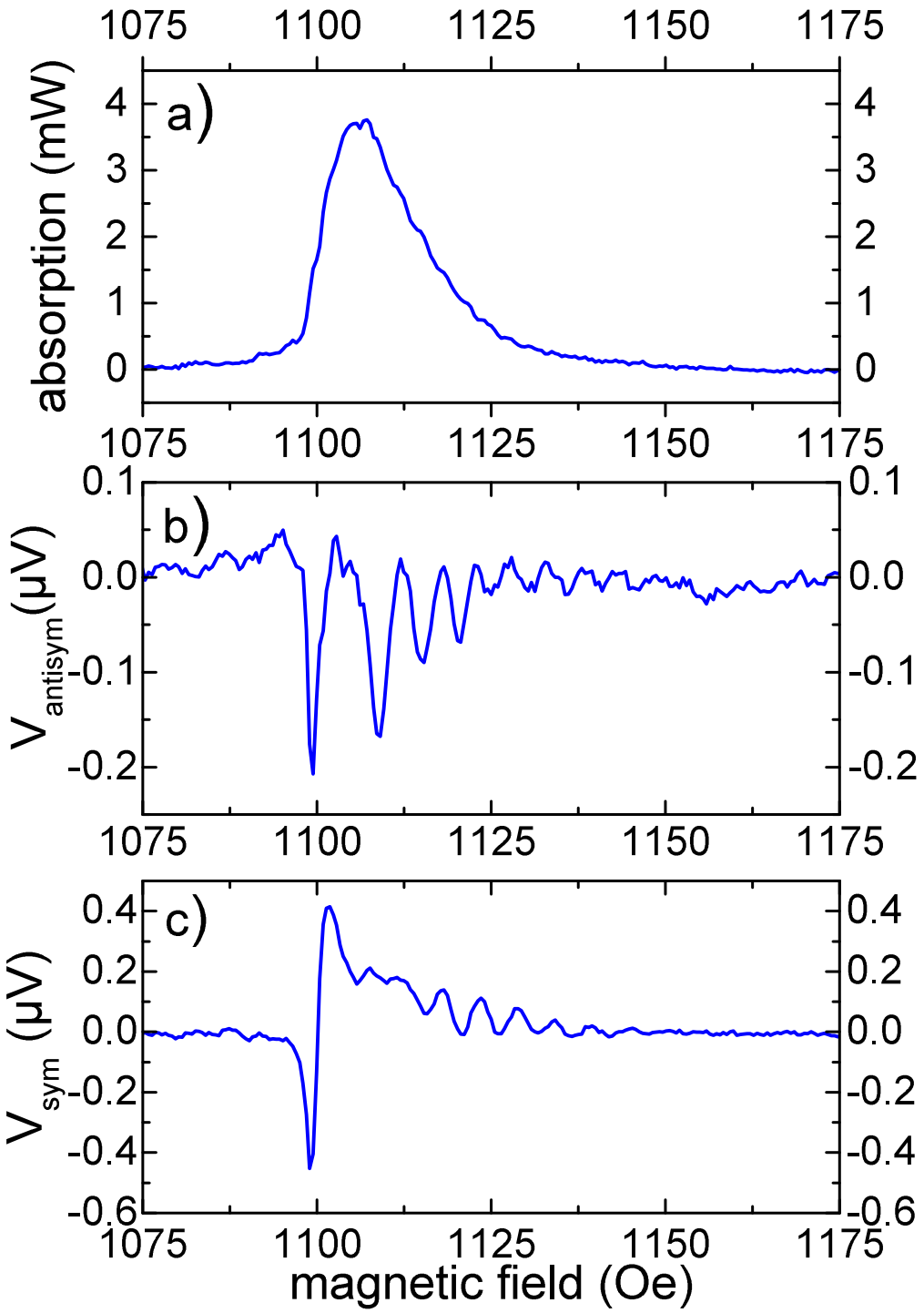

Fig. 4.14: a) Absorption, b) antisymmetric and c) symmetric voltage for in-plane magnetized bilayers for an excitation frequency of 5 GHz and an excitation power of about 31.6 mW.

the Seebeck voltage but can still be seen.

Antisymmetric voltage

As can be seen in figure 4.14b) the antisymmetric voltage is dominated by oscillations as well. This is a totally different behaviour than it was observed for out-of-plane magnetized structures. A possible origin is the interference of the direct electromagnetic wave and the spin-waves. According to Faraday's induction law [21, p.212] the total dynamic magnetic fields $\vec{b}$ can induce a voltage V_{ind} in the adjacent graphene layer:

$$V_{\mathrm{ind}} = -\frac{1}{c}\int_A \frac{\partial \vec{b}}{\partial t} \cdot d\vec{A}. \tag{4.10}$$

where $\vec{A}$ is the vector of a surface element of area A and c is the speed of light. The scalar product between the temporal derivative of the dynamic magnetic field $\vec{b}$ and the surface vector $\vec{A}$ also explains why this effect is not observed for out-of-plane magnetized structures. In this case all dynamic spin-wave components are in-plane and accordingly perpendicular to the surface vector leading to a vanishing induction by spin-waves.
The induced voltage is an ac-voltage that depends on the local amplitude of the dynamic magnetic field. The total amplitude of the induced voltage $V_i(t, d_i, H)$ at the position of the i-th contact can be estimated from sum of the spin-wave and direct wave contribution:

$$V_i(t, d_i, H) = V_i^{\mathrm{SW}}(d_i, H)\sin[\omega t + k(H)d_i + \alpha] + V_i^{\mathrm{dir}}(d_i, H)\sin[\omega t + \beta] \tag{4.11}$$

where d_i is the distance between the i-th contact and the antenna, α and β are phase terms that account for phase differences of the initial phase to the induced voltage, k is the wave vector of the spin-wave and ω is the frequency of both the direct and the spin-wave. $V_i^{\mathrm{SW}}(d_i, H)$ is the amplitude of the induction caused by the spin-wave in dependence of the distance to the antenna so that spin-wave damping is taken into account. The dependence on the applied magnetic field considers the fact that for higher magnetic fields higher wave vectors are excited with decreasing efficiency. $V_i^{\mathrm{dir}}(d_i, H)$ is the amplitude of the direct wave. It also depends on the magnetic field since for increased excitation of spin-waves the direct wave amplitude reduces as described before. A phase contribution due to the wave vector of the direct wave can be neglected since the wave length can be estimated to be several centimetres for the examined frequencies. Accordingly, the phase term is not expected to significantly change on the distance between the contacts. Using trigonometric identities [61,

p. 83] equation (4.11) can be transformed into

$$V_i(t, d_i, H) = V_i^0(d_i, H)\sin[\omega t + \varphi_i(d_i, H)] \tag{4.12}$$

with

$$\tan[\varphi_i(d_i, H)] = \frac{V_i^{\mathrm{SW}}\sin(kd_i + \alpha) + V_i^{\mathrm{dir}}\sin(\beta)}{V_i^{\mathrm{SW}}\cos(kd_i + \alpha) + V_i^{\mathrm{dir}}\cos(\beta)} \tag{4.13}$$

and

$$V_i^0(d_i, H) = \sqrt{(V_i^{\mathrm{dir}})^2 + (V_i^{\mathrm{SW}})^2 + 2V_i^{\mathrm{dir}}V_i^{\mathrm{SW}}\cos(kd_i + \alpha')} \tag{4.14}$$

with $\alpha' = \alpha - \beta$. Due to the rectification and the dc-measurement the temporal oscillation only leads to an amplitude prefactor a so the phase term φ_i and the frequency become irrelevant. Accordingly, the induced voltage in the i-th contact is given by equation (4.14) and a prefactor. Since our setup cannot detect the unrectified voltage the value of a is set to 1, and solely the sign has to be regarded in further calculations. An example of the spatial distribution of the induced voltage amplitude is shown in figure 4.15.

Calculation of the antisymmetric voltage In the following we will try to calculate the antisymmetric voltage for varying magnetic fields. Since for several estimations values have to be taken from the data this is not to be regarded as a complete prediction of the antisymmetric voltage, but as a careful approach to understand the data. Using the fact that we measure a voltage difference at the position of the two contacts $V(H) = V_1(H) - V_2(H)$ and the definition of the antisymmetric voltage in equation (4.2) we get

$$V_{\mathrm{antisym}}(H) = \mathrm{sgn}(a)\{[V_1^0(H) - V_2^0(H)] - [V_1^0(-H) - V_2^0(-H)]\}/2 \tag{4.15}$$

where V_i^0 is the induced voltage in equation (4.14) at the i-th contact and sgn(a) is the sign of the prefactor. To be able to determine the field dependence of this equation the amplitudes V_i^{dir} and V_i^{SW} are needed. The direct wave voltage can be determined from the offset. For magnetic fields far away from the FMR-field the voltage of a single field direction is solely determined by the amplitude of the direct wave. The different amplitudes of the direct wave at the position of the contacts leads to a voltage difference that can be detected by our setup. In this case the offset is (-7.8±0.1) µV. The negative sign shows that the amplitude prefactor a has to be negative. From the symmetric voltage it can be seen that the variations of the direct wave amplitude for magnetic fields that allow for spin-wave excitation is much smaller than the offset value so these variation will be neglected and the

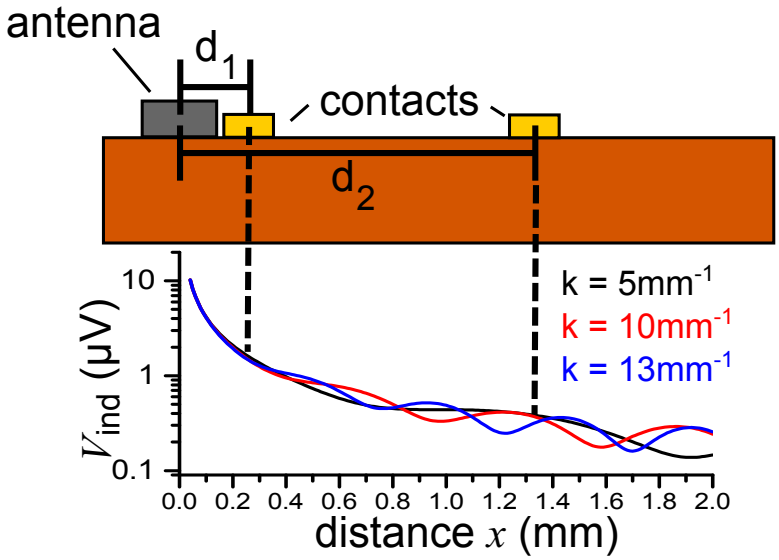

Fig. 4.15: Spatial distribution of the induced voltage amplitude calculated from equation (4.14) with $d_i{=}x$, $V_i^{\mathrm{dir}}{=}(0.405\,\mu\mathrm{V}{\cdot}\mathrm{mm})/x$ and $V_i^{\mathrm{SW}}{=}0.11\,\mu\mathrm{V}{\cdot}\exp(-x/5\,\mathrm{mm})$ for the positive field direction with and without prefactor sign (position and size of contacts and antenna only for illustration).

direct wave is independent of the magnetic field. Using the fact that the direct wave amplitude is inverse proportional to the distance from the antenna we have

$$|V_{\mathrm{Offset}}| = \frac{V_0^{\mathrm{dir}}}{d_1} - \frac{V_0^{\mathrm{dir}}}{d_2} \tag{4.16}$$

The distance d_1 and d_2 are determined to be

$$d_1 = (0.05 \pm 0.04)\,\mathrm{mm} \qquad \text{and} \qquad d_2 = (1.35 \pm 0.04)\,\mathrm{mm}. \tag{4.17}$$

From these values the amplitudes of the direct wave can be calculated

$$V_1^{\mathrm{dir}} = (8.10 \pm 0.66)\,\mu\mathrm{V} \qquad \text{and} \qquad V_2^{\mathrm{dir}} = (0.30 \pm 0.26)\,\mu\mathrm{V}. \tag{4.18}$$

In the following we will discuss the dependence of the antisymmetric voltage on the spin-wave properties. The behaviour of the cosine term in equation (4.14) is determined by the phase of the dynamic out-of-plane magnetic field of the spin-wave. While the amplitude for backward volume waves stays the same under inversion

of the static magnetic field the phase is shifted by a value of π [60] leading to a sign change of the cosine term. This way the induced voltage contributes to the antisymmetric voltage.
Additionally the cosine term depends on the wave vector of the spin-wave. The wave vectors with respect to the magnetic field can be calculated using the theory developed by Kalinikos in the diagonal approximation for low wave vectors and backward volume waves [62]:

$$\omega^2 = \gamma^2[H \cdot (H + 4\pi M_0)] - \gamma^2 H \cdot 4\pi M_0 \cdot P \tag{4.19}$$

with

$$P = 1 - \frac{1}{k \cdot t}\left[1 - \exp(-k \cdot t)\right]$$

and $t = 5.1\,\mu\text{m}$ the thickness of the YIG layer. The magnetization for YIG is $4\pi M_0 = 1750\,\text{G}$. Calculations show that the wave vector increases monotonously with increased magnetic field. Accordingly, the phase term kd_i grows for enhanced magnetic field as well and leads to oscillations of the amplitude.
It can be shown that the peak to peak amplitude of the oscillation solely depends on the amplitude of the spin-wave voltage. Since the oscillations observed for the antisymmetric voltage is determined by the distance to the second contact the peak to peak amplitude of the first peak can be used to determine the spin-wave voltage V_2^{SW}. The spin-wave voltage at the first contact is determined by assuming a exponential decay of the spin-wave with increased distance from the antenna with a decay length of $(5\pm2)\,\text{mm}$. We have

$$V_1^{\text{SW}} = (0.11 \pm 0.06)\,\mu\text{V} \qquad \text{and} \qquad V_2^{\text{SW}} = (0.08 \pm 0.02)\,\mu\text{V}. \tag{4.20}$$

Additionally the excitation efficiency of spin-waves can be reconstructed from the shape of the absorption curve $P(H)$ for magnetic fields above the FMR-field. For this task an exponential fit to the data is used

$$P(H) = P_0 \cdot \exp\left(-\frac{H - H_0}{\sigma}\right) \tag{4.21}$$

with $H_0 = (1109.2 \pm 0.5)\,\text{Oe}$ and $\sigma = (10 \pm 0.5)\,\text{Oe}$. The result is shown in figure 4.16a). Since the absorption quadratically depends on the dynamic magnetization the square root of the determined function has to be calculated. The spin-wave voltage at the i-th contact is then given by

$$V_i^{\text{SW}}(H) = V_i^{\text{SW}} \cdot \exp\left(-\frac{H - H_0}{2\sigma}\right). \tag{4.22}$$

Combining equation (4.14), (4.15) and (4.19) we get the result shown in figure 4.16b). The perfect match of the amplitude of the first peak is no surprising result since this value was taken from data. Still, for the field dependent behaviour no further values were taken from the antisymmetric voltage. Although these calculation may not be regarded as an exact prediction of the antisymmetric voltage the good agreement with the data shows that these oscillations are most certainly caused by the induction and rectification of voltages in the graphene layer.
Accordingly, it is rather unlikely that the antisymmetric voltage observed for in-plane magnetized structures is caused by the spin-wave mediated magnetoelectric effect that was proposed for out-of-plane magnetized structures. The corresponding tensor component α_{11} vanishes.

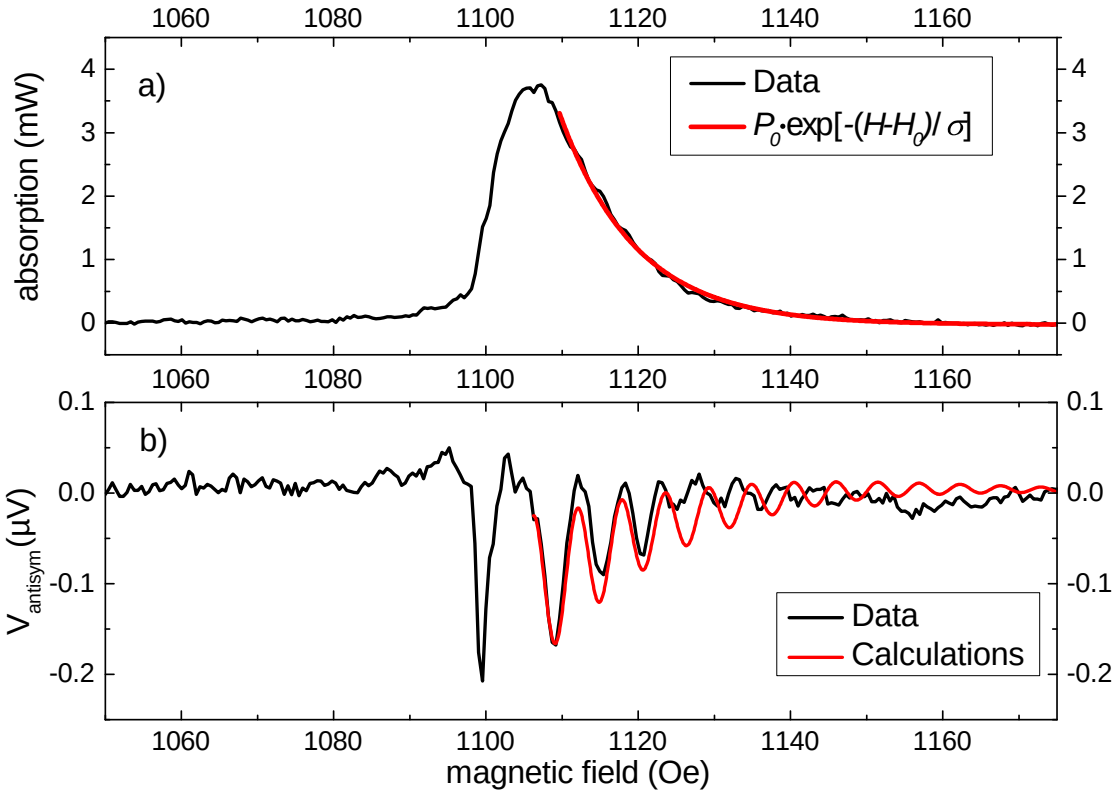

Fig. 4.16: a) Exponential fit to the absorption of microwaves for magnetic fields above the FMR-field and b) comparison of the measured antisymmetric voltage for an excitation frequency of 5 GHz and an excitation power of about 31.6 mW with the calculations of the induced voltage.

4.2.2 Transversal voltage

To determine the tensor component α_{21} the structure has to be magnetized along the direction of spin-wave propagation and the voltage is measured perpendicular to this orientation. The experimental results are shown in figure 4.17. The offset in this case is about 11.4 µV revealing a high induction by the direct wave as expected for the low distance of the contacts to the antenna. Like for out-of-plane magnetized bilayers the transversal voltage is dominated by oscillations that are caused by the reduction of the direct wave amplitude for magnetic fields that allow for increased spin-wave excitation due to transversal modes.
Again like for out-of-plane magnetized structures no antisymmetric voltage can be observed. Every variation is most certainly an uncertainty especially since these measurements were done before the technical improvements described in section 3.3. Accordingly, the spin-wave mediated magnetoelectric effect cannot be observed for backward volume waves with the voltage measured perpendicular to the direction of propagation and the tensor component α_{21}^{E} vanishes as well.

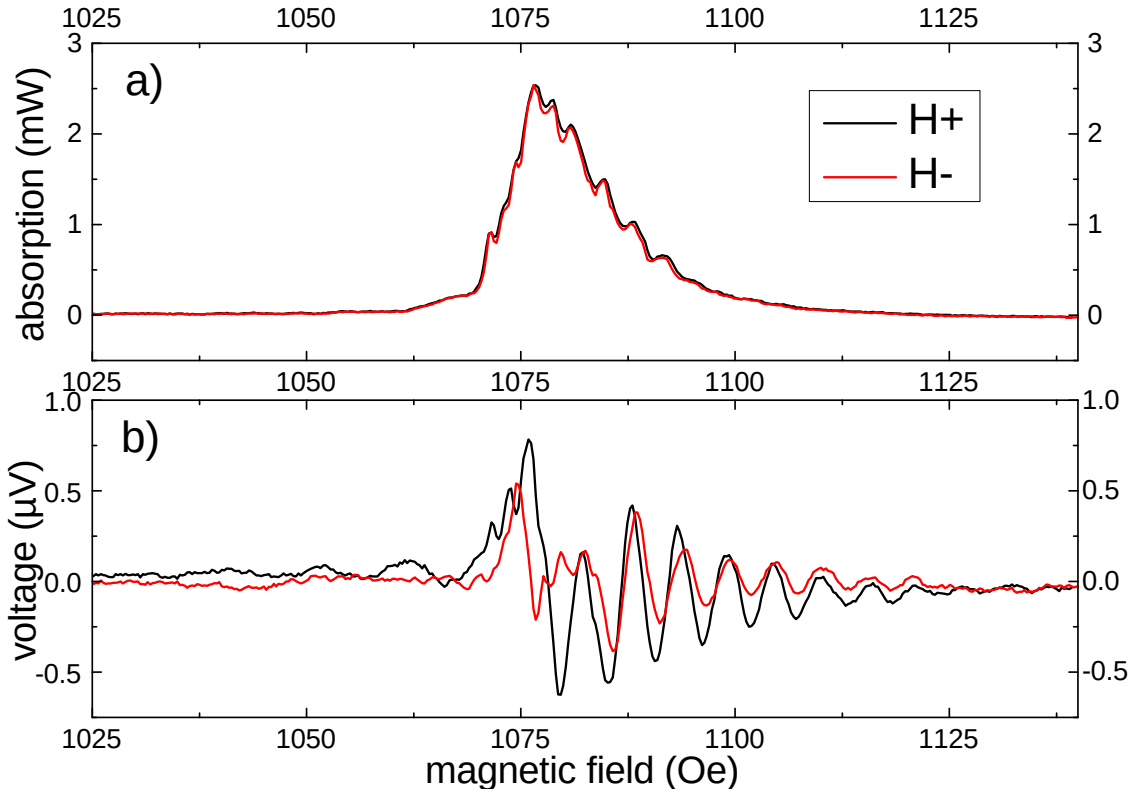

Fig. 4.17: a) Absorption and b) voltage for in-plane magnetized structures with the voltage measured perpendicular to the direction of spin-wave propagation. The excitation frequency is 6 GHz and the excitation power about 31.6 mW.

5 Discussion and outlook

In this thesis we have shown that for YIG/graphene bilayers a voltage in the graphene layer can be observed that is clearly correlated to the excitation of spin-waves in the YIG-layer. For out-of-plane magnetized structures it could be shown that the observed voltage consists of a component that reverses sign under the inversion of the orientation of the static magnetic field and one component that does not. The appearance of the symmetric voltage can be explained by two known effects:

1. A direct electromagnetic wave emitted by the antenna induces currents in the graphene layer that are rectified by a Schottky barrier between the graphene layer and the gold contacts.

2. A temperature gradient from the antenna along the direction of propagation caused by the damping of spin-waves leads to a Seebeck voltage.

For the antisymmetric voltage the situation is more complicated since no explanation seems to exist so far. In section 4.1.1 we proposed a mechanism of a spin-wave mediated magnetoelectric effect. For this we assume the magnetoelectric susceptibility tensor α_{ij} to depend on the propagation properties of spin-waves:

$$E_i = \alpha_{ij}^{\mathrm{E}}[\vec{\phi}^{\mathrm{m}}(H)] \cdot H_j. \tag{5.1}$$

The tensor $\alpha_{ij}^{\mathrm{E}}[\vec{\phi}^{\mathrm{m}}(H)]$ only shows non-vanishing values in the presence of a current of magnons $\vec{\phi}^{\mathrm{m}}[H(\omega_0)]$ which was defined to be along the x-axis. In our experiments we examined all experimentally accessible components of this tensor and found them to be determined:

$$\alpha_{11} = 0 \qquad \alpha_{13} = \alpha_{\perp}^{\mathrm{E}}(\phi^{\mathrm{m}}, \omega_0) \tag{5.2}$$

$$\alpha_{21} = 0 \qquad \alpha_{23} = 0 \tag{5.3}$$

The undetermined tensor components are very difficult or even impossible to access. The magnetic field oriented along the y-axis leads to the excitation of Damon-Eshbach modes that are non-reciprocal under the inversion of the static magnetic field. Accordingly, the results for different field directions are not comparable and the symmetric voltage and antisymmetric voltage - if present- cannot be separated. For electric fields along the z-axis it is most certainly impossible to detect a corresponding voltage since this would need for contacts below and above the graphene

layer. This would deform the graphene structure and accordingly strongly influence the electronic properties [33]. Additionally the contact to the YIG layer would be lost at this position so that the process would most certainly - if present - disappear anyway.
For the measured components we see that for in-plane magnetized structures the effect does not appear neither for an electric field measured parallel or perpendicular to the direction of spin-wave propagation or the current of magnons.
For out-of-plane magnetized structures the situation is different. Here again the effect cannot be observed for voltages measured perpendicular to $\vec{\phi}^{\mathrm{m}}$. Only for the voltage measured along the direction of spin-wave propagation non-vanishing values of the antisymmetric voltage are observed. From the results gained during this thesis a phenomenological equation can be derived:

$$\vec{E} = \alpha'_{\perp}(\omega_0)\,\vec{\phi}^{\mathrm{m}}(H) \cdot (\vec{n} \cdot \vec{H}) \tag{5.4}$$

with $\vec{n}$ as a normal unit vector to the bilayer surface and $\alpha'_{\perp}(\omega_0)$ as a proportional constant. Writing equation (5.4) in components we see that it is equivalent to equation (5.1):

$$E_i = \underbrace{\alpha'_{\perp}(\omega_0)\,\phi_i^{\mathrm{m}}(H) n_j}_{\alpha_{ij}^{\mathrm{E}}} \cdot H_j. \tag{5.5}$$

The equation matches all observations that could be made for the antisymmetric voltage:

1. The linear dependence on the vector of the magnetic field allows for reversion of the electric field under the inversion of the magnetic field.

2. The scalar product between the magnetic field and the vector $\vec{n}$ leads to vanishing voltages for in-plane magnetized YIG/graphene bilayers and to maximum values for out-of-plane orientation of the magnetic field.

3. The direction of the electric field is defined by the direction of spin-wave propagation. Accordingly, no transversal antisymmetric voltages can be detected.

4. The voltage vanishes for magnetic fields that do not allow for spin-wave excitation and is sensitive to the excitation efficiency of spin-waves due to the dependence on ϕ^{m}.

5. Due to the linear relation between the electric field and the current of magnons ϕ^{m} the linear dependence on the absorbed energy is described.

6. The dependence of $\alpha'_{\perp}$ on the excitation frequency ω_0 allows for an description of the resonant frequency dependence.

Symmetry considerations additionally show that the vector $\vec{n}$ has to be an axial vector. We proposed a screw dislocation to be the origin of this vector and $\vec{n}$ to be aligned with the displacement vector. A possible explanation is a deformation of the graphene layer due to the deformed YIG surface at the position of the dislocation. Since the electronic properties of graphene are very sensitive to deformation of the hexagonal lattice this might form an electronic state that under the influence of spin-waves leads to voltage that is antisymmetric under inversion of the static magnetic field. The difficulty with this explanation is that one would assume an identical number of screw dislocations with displacement vector parallel or antiparallel to the z-axis. Accordingly, the effect should average to zero. Still, it is possible that due to some process during sample growth one orientation is preferred leading to a non-vanishing effect. Another possibility is that only one orientation couples to the graphene layer and leads to the observed phenomena.
Still, these ideas are merely speculation and need further experiments. To examine if the effect also appears for other structures YIG/aluminium bilayers were analysed. Here no antisymmetric voltage could be observed. This can be caused by two different reasons:

1. The effect needs material properties that are given for graphene but absent in aluminium.

2. The detected voltage depends on the layer thickness of the material on YIG. Since we assume a deformation of the adjacent layer due to the presence of a screw dislocation to be the origin of the antisymmetric voltage a less pronounced or vanishing effect would be expected for increasing layer thickness.

Probably the actual reason for the vanishing antisymmetric voltage is a combination of both properties.

As one can see from this summary during this thesis many aspects of this potentially new physical effect have already been determined, but for a full understanding still many details on the origin of the antisymmetric voltage are unknown and need further experiments. A few propositions will be given in the following list:

1. To verify the idea if screw dislocations are the origin of the axial vector $\vec{n}$ it is necessary to prove the presence of screw dislocations in the YIG layer. These experiments have already begun and indicate the existence of dislocations observable at the YIG surface although the type of dislocation is still undetermined.

2. Due to the high complexity of the system which can be seen in the number of contributing effects to the detected voltage it might be helpful to simplify

the system. Since the origin of the main process of the antisymmetric voltage is assumed to be found in the behaviour of spin-waves it might be interesting to closely analyse the spin-wave properties in a YIG film without adjacent graphene layer especially under the inversion of the static magnetic field. A very simple approach would be a detailed examination of the absorption for a fixed magnetic field and an scanned excitation frequency to avoid hysteresis effects. A rotation of the bilayer in the magnetic field is then used to reverse the relative orientation of the magnetic field. These experiments have also begun and indicate a shift of the resonance peak with respect to the static magnetic field.
Especially a phase sensitive analysis using a Brillioun light scattering setup [63] would be interesting but up to now this is technically rather difficult for out-of-plane magnetized structures.

3. A reduction or elimination of the direct electromagnetic wave would most certainly improve the data situation for in-plane magnetized structures and clearly reveal that no antisymmetric voltage is present in this configuration. Additionally the reduced amplitude of the direct wave for magnetic fields that allow for spin-wave excitation influences every detected symmetric voltage so that statements for example about the power dependence of the amplitude are quite difficult. The reduction could be achieved by the usage of a coplanar antenna instead of a stripline antenna. This way the dynamic magnetic field is only excited locally and the amplitude of a direct wave could be significantly reduced or even removed.
The preparations for these experiments have already begun as well and the experiments will start in the near future.

In conclusion, we see that the combination of YIG and graphene in a bilayer leads to very interesting behaviour under the influence of spin-wave excitation, and accordingly fulfils our expectations. The detected voltage in the graphene layer could be determined to strongly depend on the presence and amplitude of spin-waves excited in the YIG layer. While some of the observed phenomena could be explained by known effects, like the Seebeck effect, others are still open to discussion. The most interesting observation is the appearance of a voltage component, measured along the direction of spin-wave propagation, that for out-of-plane magnetized structures reverses sign under inversion of the static magnetic field. To our best of knowledge, this cannot be explained by any known effect so far. As a first attempt to describe this observation we proposed a spin-wave mediated magnetoelectric effect that due to its symmetry properties could be connected to the presence of screw dislocations in the YIG layer.

A Appendix

A.1 Calibration of microwave signals

The calibration of microwave signals has to be separated in two steps:

1. Calibration of the microwave detectors
2. Calibration of the attenuator of the reflection signal

A.1.1 Calibration of the microwave detectors

In the first step the microwave detectors are connected to the microwave generator. The output of the microwave detectors is a negative voltage that is measured using the oscilloscope. For frequencies from 2 to 9 GHz in a frequency step width of 0.02 GHz the power is varied from 0.01 mW to 10 mW. For each frequency the output power of the microwave generator is plotted against the measured voltage with reversed sign (see figure A.1).

The datasets are fitted with a quadratic function.

$$P(U_0) = P_0 + \left.\frac{\partial P}{\partial U}\right|_{U=U_0} \cdot U + \left.\frac{\partial^2 P}{\partial U^2}\right|_{U=U_0} \cdot U^2 \tag{A.1}$$

The corresponding parameters all have very similar values for different frequencies. Due to the large number of measurements only the mean values are shown in table A.1. The values show that both detectors are very similar as expected.

A.1.2 Calibration of the microwave attenuators

In our setup we use a directional coupler to measure the reflection signal. According to the manufacturer the reflected signal is attenuated by 10 dBm. Since this value is actually frequency depended a calibration is needed. Therefore a network analyser is used for frequencies from 1.5-10 GHz in a step width of about 5.3 MHz. The attenuation varies from 9.36 dBm to 12.97 dBm with a mean value of 11.11 dBm. In the analysis program the exact values are implemented. For frequencies that have

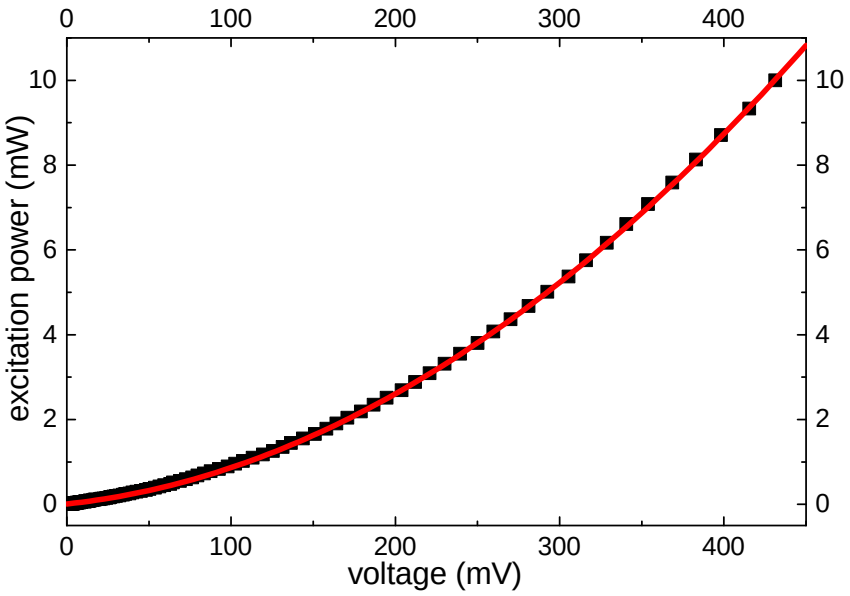

Fig. A.1: Calibration of the microwave detectors. Applied microwave power displayed against measured voltage for 5 GHz.

not been measured in the calibration a linear interpolation is used.
For the attenuation in mW we have:

$$P_{\mathrm{dBm}} - A_{\mathrm{dBm}} = 10\,\mathrm{dBm} \cdot \left[\log\left(\frac{P_{\mathrm{mW}}}{1\,\mathrm{mW}}\right) - \log(x)\right] \tag{A.2}$$

$$\Rightarrow P_{\mathrm{mW}} = x \cdot P_{\mathrm{measured/mW}} \qquad \text{and} \qquad x = 10^{A_{\mathrm{dBm}}/10\,\mathrm{dBm}} \tag{A.3}$$

where P_{dBm} and P_{mW} are the microwave power in dBm and mW, A_{dBm} is the attenuation in dBm and x defines the attenuation factor.

	transmission detector	reflection detector
P_0 [mW]	9.98×10^{-3}	1.15×10^{-2}
$\frac{\partial P}{\partial U}\Big\vert_{U=U_0}$ [mW/mV]	4.26×10^{-3}	4.43×10^{-3}
$\frac{\partial^2 P}{\partial U^2}\Big\vert_{U=U_0}$ [mW/mV^2]	4.30×10^{-5}	4.34×10^{-5}

Tab. A.1: Mean value of calibration parameters (quadratic fit) of the microwave detectors in a frequency range from 2-9 GHz for the transmission and reflection detector.

A.2 Calibration of the magnetic field

For the calibration of the magnetic field two different methods were used. The first uses a Hall probe to measure the magnetic field for an applied current in the electromagnet. The best agreement with the data shown in figure A.2 can be achieved using a third order polynom

$$H(I) = H_0 + H_1 \cdot I + H_2 \cdot I^2 + H_3 \cdot I^3 \tag{A.4}$$

with the parameters

$$H_0 = 47.8\,\mathrm{Oe} \tag{A.5}$$
$$H_1 = 220.8\,\mathrm{Oe/A} \tag{A.6}$$
$$H_2 = 2.95\,\mathrm{Oe/A^2} \tag{A.7}$$
$$H_3 = -0.11\,\mathrm{Oe/A^3}. \tag{A.8}$$

The results are shown in figure A.2.
To check the quality of the calibration spin-waves are excited in out-of-plane magnetized YIG/graphene bilayers with several excitation frequencies and the magnetization is calculated using equation (2.21). The magnetization is determined from the maximum of absorption. We see that for currents between 3 A and 6.5 A the magnetization is reproduced quite good (1750±30 G). The uncertainty accounts for possible anisotropies. For higher currents strong variations for different excitation frequencies and so for different static magnetic fields are observed. An explanation could be that the Hall probe was not placed close enough to the position of the YIG/graphene bilayer. Still, this calibration is sufficient for measurements with in-plane magnetized structures since this matches the interval of the needed magnetic fields.
For the out-of plane magnetized fields (10 A to 20 A) another calibration is necessary. Therefore, a YIG sample was placed in the sample holder. For out-of-plane magnetized structures the sample was connected to a network analyser[1]. For every applied current the resonance frequency was detected. This way the magnetic field can be calculated using the Kittel formula (see (2.21)):

$$H(I) = \frac{\omega}{\gamma} - 4\pi M_z \tag{A.9}$$
$$\Rightarrow H_0 + H_1 \cdot I = \frac{\omega}{\gamma} - 4\pi M_z. \tag{A.10}$$

The magnetization was assumed to be 1750±30 G. The corresponding data is shown in figure A.3. The calibration parameters can be determined using a linear fit. The

[1] type: Agilent E5071C ENA Series Network Analyser

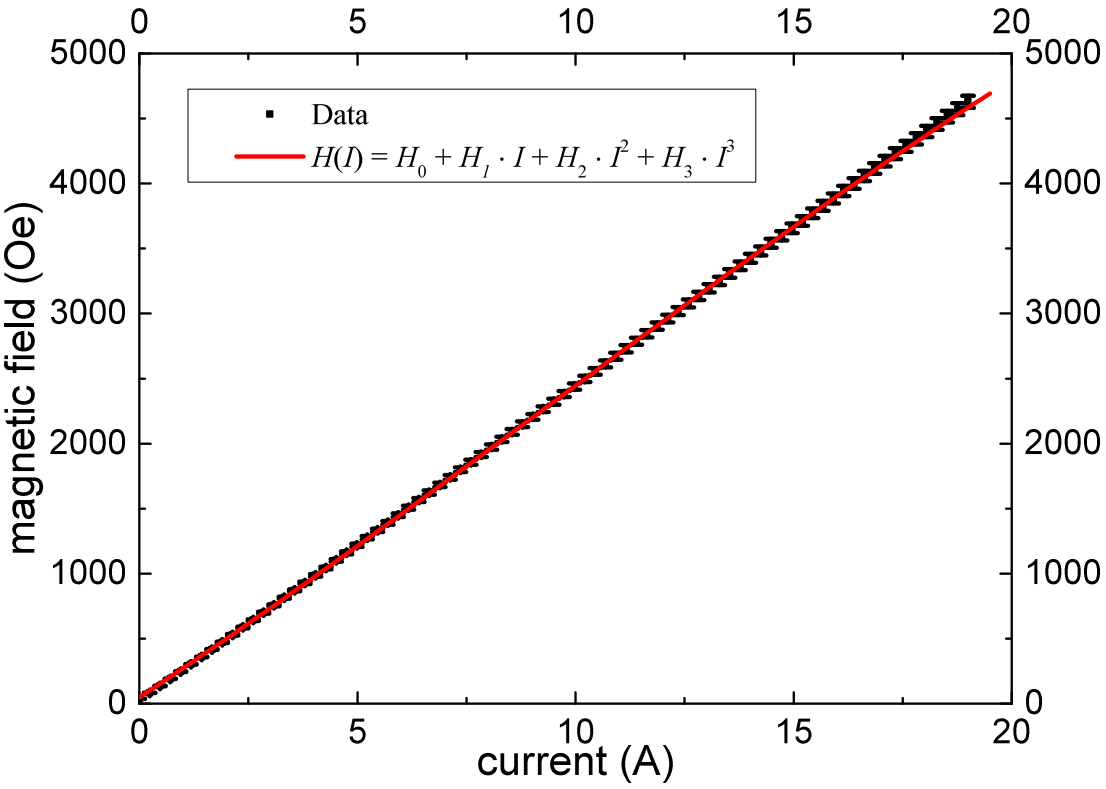

Fig. A.2: Magnetic field detected with a Hall probe displayed against the current in the electromagnet. The data points (black) are described by a third order polynom fit (red).

parameters averaged for both directions of the magnetic field are

$$H_0 = 115.869\,\text{Oe} \tag{A.11}$$
$$H_1 = 247.6765\,\text{Oe/A}. \tag{A.12}$$

This calibration shows very good agreement with the data measured in later experiments. Only for currents close to 10 A small deviations of the magnetization from 1750 G can be observed.

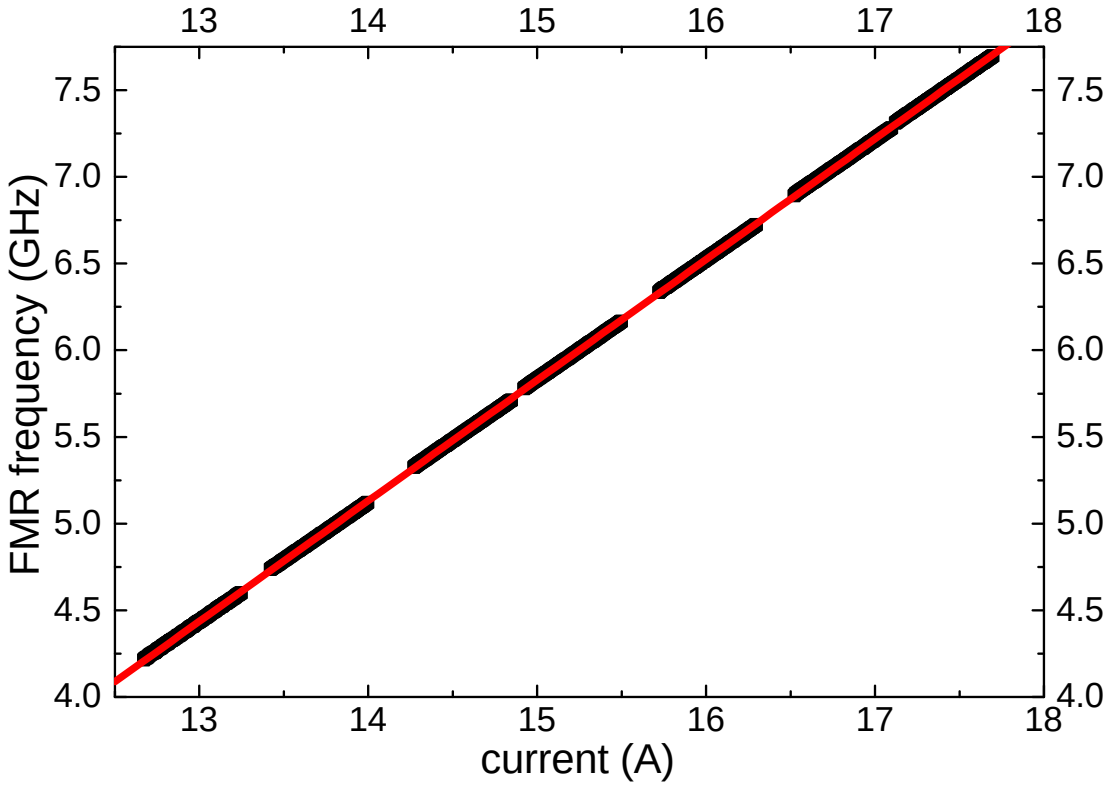

Fig. A.3: FMR frequency displayed against the electric current of the electromagnet. The data (black) consists of set of about 300 points determined for the negative field direction. The red curve is a linear fit using equation (A.10).

Danksagung

Am Ende dieser Arbeit möchte ich allen Danken, die zu einem Gelingen dieses Projektes beigetragen haben.
Zu Beginn möchte ich Prof. Dr. Sergej O. Demokritov dafür danken, dass er es mir ermöglicht hat an diesem spannenden und fordernden Thema zu arbeiten. Auch für seine jederzeit hilfreichen Anregungen bin ich sehr dankbar.
Ein besonderer Dank geht an meinen Betreuer Dr. Oleksandr Dzyapko mit dem ich gemeinsam an diesem Projekt gearbeitet habe und auch weiterhin arbeiten werde. In zahlreichen Diskussionen konnte ich viel über Spinwellen und die damit verbundene experimentelle Methodik lernen und meine eigenen Ideen einbringen.
Auch möchte ich Dr. Vladislav E. Demidov und Philipp Seibt danken, die beide stets ihre Arbeit sofort unterbrochen haben um meine zahlreichen Fragen zu beantworten, seien sie nun physikalischer oder grundsätzlicher Natur.
Abschließend danke ich meiner Familie und meinen Freunden, die mir in dieser arbeitsintensiven Zeit immer unterstützend und oftmals geduldig zur Seite gestanden haben. Ganz besonders danke ich hier meiner Freundin Lisa, die mich auch in schwierigeren Zeiten immer wieder ermutigt hat und wieder aufgebaut hat.
Dafür an alle Beteiligten ein ganz herzliches Dankeschön!

Plagiatserklärung

Hiermit versichere ich Michael Evelt, dass die vorliegende Arbeit mit dem Titel "Spin-wave mediated magnetoelectric effect in YIG/graphene bilayers" selbstständig verfasst worden ist, dass keine anderen Quellen und Hilfsmittel als die angegebenen benutzt worden sind und dass die Stellen der Arbeit, die anderen Werken - auch elektronischen Medien - dem Wortlaut oder Sinn nach entnommenen wurden, auf jeden Fall unter Angabe der Quelle als Entlehnung kenntlich gemacht worden sind.

Münster, 29. April 2015

Ich erkläre mich mit einem Abgleich der Arbeit mit anderen Texten zwecks Auffindung von Übereinstimmungen sowie mit einer zu diesem Zweck vorzunehmenden Speicherung der Arbeit in eine Datenbank einverstanden.

Münster, 29. April 2015

Literaturverzeichnis

[1] M. Fiebig, "Revival of the magnetoelectric effect," *J. Phys. D: Appl. Phys.*, vol. 38, p. R123, Feb. 2005.

[2] A. Gurevich and G. Melkov, *Magnetization Oscillations and Waves*. CRC Press, 1996.

[3] V. V. Kruglyak, S. O. Demokritov, and D. Grundler, "Magnonics," *J. Phys. D: Appl. Phys.*, vol. 43, no. 26, p. 264001, 2010.

[4] K. S. Novoselov, A. K. Geim, S. V. Morozov, D. Jiang, Y. Zhang, S. V. Dubonos, I. V. Grigorieva, and A. A. Firsov, "Electric Field Effect in Atomically Thin Carbon Films," *Science*, vol. 306, no. 5696, pp. 666–669, 2004.

[5] K. S. Novoselov, A. K. Geim, S. V. Morozov, D. Jiang, M. I. Katsnelson, I. V. Grigorieva, S. V. Dubonos, and A. A. Firsov, "Two-dimensional gas of massless Dirac fermions in graphene," *Nature*, vol. 438, pp. 197–200, Nov. 2005.

[6] K. Uchida, S. Takahashi, K. Harii, J. Ieda, W. Koshibae, K. Ando, S. Maekawa, and E. Saitoh, "Observation of the spin Seebeck effect," *Nature*, vol. 455, no. 7214, pp. 778 – 781, 2008.

[7] J. Xiao, G. E. W. Bauer, K.-c. Uchida, E. Saitoh, and S. Maekawa, "Theory of magnon-driven spin Seebeck effect," *Phys. Rev. B*, vol. 81, p. 214418, Jun 2010.

[8] J. Stöhr and H. Siegmann, *Magnetism - From Fundamentals to Nanoscale Dynamics*. Springer, 2006.

[9] C. Kittel, *Einführung in die Festkörperphysik*. Oldenbourg, 14th ed., 2006.

[10] H. Ibach and H. Lüth, *Festkörperphysik*. Springer, 7st ed., 2009.

[11] W. Heisenberg, "Zur Theorie des Ferromagnetismus," *Z. Phys.*, vol. 49, no. 9-10, pp. 619–636, 1928.

[12] L. Landau and E. Lifshitz, "On the theory of the dispersion of magnetic permeability in ferromagnetic bodies," *Phys. Z. Sowietunion*, vol. 8, pp. 153–169, 1935.

[13] T. Gilbert, "A lagrangian formulation of the gyromagnetic equation of the magnetization field," *Phys. Rev.*, vol. 100, p. 1243, 1955. [Abstract only; full report, Armor Research Foundation Project No. A059, Supplementary Report, May 1, 1956].

[14] T. Gilbert, "A Phenomenological Theory of Damping in Ferromagnetic Materials," *IEEE Trans. Magn.*, vol. 40, pp. 3443–3449, Nov. 2004.

[15] V. Demidov and S. Demokritov, "Einführung in die Magnonik," 2014. Lecture at Westfälische Wilhelms-Universität Münster.

[16] J. MacDonald, "Ferromagnetic Resonance and the Internal Field in Ferromagnetic Materials," *Proc. Phys. Soc. A*, vol. 64, pp. 968–983, 1951.

[17] C. Kittel, "On the Theory of Ferromagnetic Resonance Absorption," *Phys. Rev.*, vol. 73, pp. 155–161, Jan. 1948.

[18] C. Herring and C. Kittel, "On the Theory of Spin Waves in Ferromagnetic Media," *Phys. Rev.*, vol. 81, pp. 869–880, Mar. 1951.

[19] R. Damon and J. Eshbach, "Magnetostatic modes of a ferromagnet slab," *J. Phys. Chem. Solids*, vol. 19, no. 3-4, pp. 308 – 320, 1961.

[20] M. van der Vegte, *Competing interactions in multiferroics and low-dimensional systems*. PhD thesis, University of Groningen, 2010.

[21] L. Landau and E. Lifshitz, *Electrodynamics of Continuous Media. Vol. 8*. Pergamon Press, 2nd ed., 1984.

[22] W. Nolting, *Grundkurs Theoretische Physik 3 - Elektrodynamik*. Springer, 9th ed., 2011.

[23] W. F. Brown, R. M. Hornreich, and S. Shtrikman, "Upper Bound on the Magnetoelectric Susceptibility," *Phys. Rev.*, vol. 168, pp. 574–577, Apr 1968.

[24] B. Krichevtsov, V. Pavlov, and R. Pisarev, "Giant linear magnetoelectric effect in garnet ferrite films," *JETP Letters*, vol. 49, p. 1243, Apr. 1989.

[25] S. Hayami, H. Kusunose, and Y. Motome, "Toroidal order in metals without local inversion symmetry," *Phys. Rev. B*, vol. 90, p. 024432, Jul 2014.

[26] A. H. Arkenbout, T. T. M. Palstra, T. Siegrist, and T. Kimura, "Ferroelectricity in the cycloidal spiral magnetic phase of $MnWO_4$," *Phys. Rev. B*, vol. 74, p. 184431, Nov 2006.

[27] J. Ryu, S. Priya, K. Uchino, and H.-E. Kim, "Magnetoelectric Effect in Composites of Magnetostrictive and Piezoelectric Materials," *J. Electroceram.*, vol. 8, no. 2, pp. 107–119, 2002.

[28] D. R. Tilley and J. F. Scott, "Frequency dependence of magnetoelectric phenomena in $BaMnF_4$," *Phys. Rev. B*, vol. 25, pp. 3251–3260, Mar 1982.

[29] S. Shastry, G. Srinivasan, M. Bichurin, V. Petrov, and A. Tatarenko, "Microwave magnetoelectric effects in single crystal bilayers of yttrium iron garnet and lead magnesium niobate-lead titanate," *Phys. Rev.*, vol. 70, p. R123, Aug. 200.

[30] N. Cai, C.-W. Nan, J. Zhai, and Y. Lin, "Large high-frequency magnetoelectric response in laminated composites of piezoelectric ceramics, rare-earth iron alloys and polymer," *Appl. Phys. Lett.*, vol. 84, no. 18, pp. 3516–3518, 2004.

[31] G. Srinivasan, E. T. Rasmussen, and R. Hayes, "Magnetoelectric effects in ferrite-lead zirconate titanate layered composites: The influence of zinc substitution in ferrites," *Phys. Rev. B*, vol. 67, p. 014418, Jan 2003.

[32] M. O. Goerbig, "Electronic properties of graphene in a strong magnetic field," *Rev. Mod. Phys.*, vol. 83, pp. 1193–1243, Nov 2011.

[33] N. O. Weiss, H. Zhou, L. Liao, Y. Liu, S. Jiang, Y. Huang, and X. Duan, "Graphene: An Emerging Electronic Material," *Adv. Mat.*, vol. 24, no. 43, pp. 5782–5825, 2012.

[34] J. Sun, N. Lindvall, M. T. Cole, K. Angel, T. Wang, K. Teo, D. H. Chua, J. Liu, and A. Yurgens, "Low Partial Pressure Chemical Vapor Deposition of Graphene on Copper," *IEEE Trans. Nanotechnol.*, vol. 11, pp. 255–260, March 2012.

[35] S. P. Koenig, N. G. Boddeti, M. L. Dunn, and J. S. Bunch, "Ultrastrong adhesion of graphene membranes," *Nat. Nano.*, vol. 6, pp. 543–546, Aug. 2011.

[36] T. Yoon, W. C. Shin, T. Y. Kim, J. H. Mun, T.-S. Kim, and B. J. Cho, "Direct Measurement of Adhesion Energy of Monolayer Graphene As-Grown on Copper and Its Application to Renewable Transfer Process," *Nano Lett.*, vol. 12, no. 3, pp. 1448–1452, 2012. PMID: 22335825.

[37] G. Giovannetti, P. A. Khomyakov, G. Brocks, V. M. Karpan, J. van den Brink, and P. J. Kelly, "Doping Graphene with Metal Contacts," *Phys. Rev. Lett.*, vol. 101, p. 026803, Jul 2008.

[38] M. Sepioni, R. R. Nair, S. Rablen, J. Narayanan, F. Tuna, R. Winpenny, A. K. Geim, and I. V. Grigorieva, "Limits on Intrinsic Magnetism in Graphene," *Phys. Rev. Lett.*, vol. 105, p. 207205, Nov 2010.

[39] R. R. Nair, M. Sepioni, I.-L. Tsai, O. Lehtinen, J. Keinonen, A. Krasheninnikov, T. Thomson, , A. K. Geim, and I. V. Grigorieva, "Spin-half paramagnetism in graphene induced by point defects," *Nature Phys.*, vol. 8, pp. 199–202, Jan 2012.

[40] H. J. Levinstein, S. Licht, R. W. Landorf, and S. L. Blank, "Growth of High Quality Garnet Thin Films from Supercooled Melts," *Appl. Phys. Lett.*, vol. 19, no. 11, pp. 486–488, 1971.

[41] E. A. Giess, J. D. Kuptsis, and E. A. D. White, "Liquid phase epitaxial growth of magnetic garnet films by isothermal dipping in a horizontal plane with axial rotation," *J. Cryst. Growth*, vol. 16, pp. 36–42, Oct. 1972.

[42] C. J. L. de la Rosa, J. Sun, N. Lindvall, M. T. Cole, Y. Nam, M. Löffler, E. Olsson, K. B. K. Teo, and A. Yurgens, "Frame assisted H_2O electrolysis induced H_2 bubbling transfer of large area graphene grown by chemical vapor deposition on Cu," *Appl. Phys. Lett.*, vol. 102, no. 2, pp. –, 2013.

[43] J. Sun, Y. Nam, N. Lindvall, M. T. Cole, K. B. K. Teo, Y. Woo Park, and A. Yurgens, "Growth mechanism of graphene on platinum: Surface catalysis and carbon segregation," *Appl. Phys. Lett.*, vol. 104, no. 15, p. 152107, 2014.

[44] 2015. Private communication with August Yurgens, Quantum Device Physics Laboratory Department of Microtechnology and Nanoscience Chalmers University of Technology, Göteborg, Sweden.

[45] H. Ulrichs. Graphic created for this thesis.

[46] *About Lock-In Amplifiers*. Stanford Research Systems, Mar. 2015.

[47] C. Elliott, V. Vijayakumar, W. Zink, and R. Hansen, "National Instruments LabVIEW: A Programming Environment for Laboratory Automation and Measurement," *J. Assoc. Lab. Autom.*, vol. 12, no. 1, pp. 17–24, 2007.

[48] Cygwin, *Cygwin User's Guide*, 1.73.30 ed., 2015.

[49] Ametek Advance Measurement Technology, Inc., *Model 5209, Single Phase Lock-in Amplifier, Instruction Manual*, 2002.

[50] G. Bohm and G. Zech, *Introduction to statistics and data analysis for physicists*. Deutsches Elektronen-Synchrotron in der Helmholtz-Gemeinschaft, 2010.

[51] Origin (OriginLab, Northampton, MA).

[52] CERN, *Root User's Guide*, 5.34/18 ed., Mar 2014.

[53] V. E. Demidov, M. P. Kostylev, K. Rott, P. Krzysteczko, G. Reiss, and S. O. Demokritov, "Excitation of microwaveguide modes by a stripe antenna," *Appl. Phys. Lett.*, vol. 95, no. 11, pp. –, 2009.

[54] Y. Ye, Y. Dai, L. Dai, Z. Shi, N. Liu, F. Wang, L. Fu, R. Peng, X. Wen, Z. Chen, Z. Liu, and G. Qin, "High-Performance Single CdS Nanowire (Nanobelt) Schottky Junction Solar Cells with Au/Graphene Schottky Electrodes," *ACS Appl. Mater. Interfaces*, vol. 2, no. 12, pp. 3406–3410, 2010. PMID: 21058686.

[55] Y. M. Zuev, W. Chang, and P. Kim, "Thermoelectric and Magnetothermoelectric Transport Measurements of Graphene," *Phys. Rev. Lett.*, vol. 102, p. 096807, Mar 2009.

[56] R. Gross, *Festköerperphysik*. De Gruyter, 2012.

[57] A. V. Da Rosa, *Fundamentals of Renewable Energy Processes*. Academic Press, 3rd ed., 2013.

[58] X. Liu, D. Wang, P. Wei, L. Zhu, and J. Shi, "Effect of carrier mobility on magnetothermoelectric transport properties of graphene," *Phys. Rev. B*, vol. 86, p. 155414, Oct 2012.

[59] M. Bareiß, A. Hochmeister, G. Jegert, U. Zschieschang, H. Klauk, R. Huber, D. Grundler, W. Porod, B. Fabel, G. Scarpa, and P. Lugli, "Printed array of thin-dielectric metal-oxide-metal (MOM) tunneling diodes," *J. Appl. Phys.*, vol. 110, no. 4, 2011.

[60] T. Schneider, A. A. Serga, T. Neumann, B. Hillebrands, and M. P. Kostylev, "Phase reciprocity of spin-wave excitation by a microstrip antenna," *Phys. Rev. B*, vol. 77, p. 214411, Jun 2008.

[61] I. Bronstein, K. Semendjajew, G. Musiol, and H. Mühlig, *Taschenbuch der Mathematik*. Harri Deutsch, 7th ed., 2008.

[62] B. Kalinikos, "Excitation of propagating spin waves in ferromagnetic films," *IEE Proc. H*, vol. 127, pp. 4–, Feb. 1980.

[63] A. A. Serga, T. Schneider, B. Hillebrands, S. O. Demokritov, and M. P. Kostylev, "Phase-sensitive Brillouin light scattering spectroscopy from spin-wave packets," *Appl. Phys. Lett.*, vol. 89, no. 6, 2006.